The Complex Space Weather Events of September 2017

Rajkumar Hajra[1, *], Bruce T. Tsurutani[2], and Gurbax S. Lakhina[3]

[1]National Atmospheric Research Laboratory, Gadanki, India
[2]Jet Propulsion Laboratory, California Institute of Technology, Pasadena, California, USA
[3]Indian Institute of Geomagnetism, Navi Mumbai, India

[*]Corresponding author: Rajkumar Hajra (rajkumarhajra@yahoo.co.in)

Key Points

- Extreme space weather events can occur during a descending-to-minimum phase of a solar cycle
- Varying geomagnetic impacts of interplanetary shocks, waves, HCSs/HPSs, sheaths, MCs, CIRs and HSSs are studied and explained
- Solar sources and interplanetary characters of the space weather events are identified

Abstract

The complex magnetospheric and ionospheric events during September 2017 are studied. There were 4 X-class, 27 M-class and numerous C-class flares related to ~68 coronal mass ejections (CMEs), 4 of which were halo CMEs. Of the 4 halo CMEs, only 3 reached the Earth. A fast interplanetary-CME (ICME) created an upstream sheath that caused an intense magnetic storm (SYM-H peak = -146 nT). This was followed by another intense storm (SYM-H peak = -115 nT) caused by the magnetic cloud (MC) portion of the ICME. Two moderate storms (with SYM-H peaks of -65 nT and -74 nT) were caused by a sheath associated with another halo CME and a corotating interaction region (CIR), respectively. The solar wind high-speed streams (HSSs) led to continuous substorm and convection events but no magnetic storms. Fast forward shocks (FSs) and reverse waves (RWs) associated with the fast CMEs and CIRs, and heliospheric current sheet/heliospheric plasma sheet encounters were detected. The FSs and RWs caused positive and negative sudden impulses, respectively. Half of the FSs triggered substorm onsets and the RWs caused substorm recovery phases. While the FSs led to magnetospheric relativistic electron decreases, electron accelerations were associated with the MC and the HSSs. During main phases of the intense storms, two supersubstorms (SSSs) were detected, one triggered by a FS and the other by a non-shock ram pressure pulse. The SSSs caused major geomagnetically induced currents. CME propagation codes were tested with errors in arrival times ranging from ~24 min to > 35 h.

Keywords

Solar flare; CME/ICME; CIR; Interplanetary shock; HCS/HPS; Substorm

1. Introduction

The goal of this work is to comprehensively explore the geoeffectiveness of the space weather events during the entire month of September 2017, an extremely active solar interval. Although this interval was in a descending-to-minimum phase of a solar cycle (SC), this was characterized by multiple solar and interplanetary events, such as 4 X-class, 27 M-class and numerous C-class solar flares, and ~68 coronal mass ejections (CMEs) including 4 halo events. There were 3 coronal holes (CHs) emitting high-speed (defined as Vsw > 550 km s^{-1}) streams (HSSs) during the interval. This multitude of solar activity filled interplanetary space between the Sun and 1 AU.

While some aspects of the extreme flares during this interval and their effects have been reported in the literature (e.g., Chamberlin et al., 2018; Chertok et al., 2018; Schillings et al., 2018; Shen et al., 2018; Yan et al., 2018; Zou et al., 2019), there is no complete study on the complex space weather events during this entire month. This solar activity and the consequential space weather effects are particularly interesting because of the phase of the solar cycle that they occurred in. As an example, Tsurutani et al. (1992), Echer et al. (2008) and Meng et al. (2019) have noted the occurrence of superstorms (with Dst/SYM-H peak ≤ -250 nT) during solar minimum and the solar ascending phase. Although no superstorm occurred during this interval of study, the solar and interplanetary complexity of this interval makes it a compelling study which will lead to better understanding of space weather overall.

Fast interplanetary CMEs (ICMEs) generate antisunward shocks and sheaths of compressed, heated and turbulent solar wind plasma and large amplitude magnetic field variations (e.g., Kennel et al., 1985; Tsurutani et al., 1988). Shocks can trigger substorms (Akasofu & Chao, 1980; Zhou & Tsurutani, 2001; Meurant et al., 2005; Hajra & Tsurutani, 2018a). Extremely intense substorms or supersubstorms (SSSs: Tsurutani et al., 2015; Hajra et al., 2016; Hajra & Tsurutani, 2018a) have been speculated to cause geomagnetically induced currents (GICs) at the Earth. If the interplanetary sheaths contain southward interplanetary magnetic field (IMF) components, they can create magnetic storms (Tsurutani et al., 1988; Zhang et al., 2007; Echer et al., 2008; Meng et al., 2019) through the process of magnetic reconnection (Dungey, 1961). It is also well-known that the magnetic cloud (MC: Burlaga et al., 1981; Klein & Burlaga, 1982) portions of ICMEs can also create magnetic storms if they contain southward IMFs (Gonzalez et al., 1994). HSSs interacting with upstream slow-speed (~350-400 km s^{-1}) streams lead to the creation of interplanetary compressed regions called corotating interaction regions (CIRs: Smith & Wolfe, 1976; Pizzo, 1985; Balogh et al., 1999). CIRs can cause magnetic storms which are generally weak in intensity because of the highly fluctuating IMF Bz therein (Tsurutani et al., 1995). However, their trailing HSS proper can create high-intensity long-duration continuous AE activity (HILDCAA: Tsurutani & Gonzalez, 1987; Tsurutani et al. 2006). HILDCAAs have been reported to be associated with the acceleration of magnetospheric relativistic electrons (e.g., Hajra et al., 2014) in the outer zone radiation belt (Van Allen & Frank, 1959). The losses of these relativistic magnetospheric electrons has also been ascribed to both interplanetary (e.g., Tsurutani et al., 2016) and magnetospheric causes (Baker et al., 1994; Horne et al., 2009; Hudson et al., 2014; Hajra & Tsurutani, 2018b). These latter two topics will also be explored in this paper.

Several empirical models (e.g., Gopalswamy et al., 2001; Michalek et al., 2004) are available in literature to predict the propagation of CMEs from the Sun to Earth. The predicted time delays and the accuracy of being able to identify the flares/CMEs responsible for the shocks/ICMEs at Earth will be tested by applying these codes to the available data.

We will study space weather features, from the Sun to the Earth's ionosphere for the month of September 2017. In attempting to do this we will first have to identify the main plasma and magnetic field features in the solar wind and then relate them to the features in the magnetosphere and ionosphere to determine if they are geoeffective or not. In doing so we will be following a technique that was used by Tsurutani et al. (1988), Gonzalez et al. (1989) and Tang et al. (1989) where one first studies geomagnetic activity at the Earth and then work backwards to interplanetary space and then to the Sun. We will also test propagation codes which relate the solar flares/CMEs to ICMEs detected at 1 AU as mentioned above.

2. Data and Method of Analyses

Solar Flares, CMEs and CHs

Space weather events occurring during September 2017 are explored in this work. To detect the solar flares, we use the X-ray fluences measured by the Solar X-ray Imager (SXI) onboard the Geostationary Operational Environmental Satellite 15 (GOES 15: Onsager et al., 1996). These data can be found at: https://www.goes.noaa.gov/. The CMEs are observed by the Large Angle and Spectrometric Coronagraph (LASCO) onboard the Solar and Heliospheric Observatory (SOHO: Domingo et al., 1995) (https://sohowww.nascom.nasa.gov/). The solar coronal images taken by the Atmospheric Imaging Assembly (AIA: Lemen et al., 2012) telescope onboard the NASA Solar Dynamics Observatory (SDO) are utilized to identify CHs (https://sdo.gsfc.nasa.gov/).

We will estimate the probable propagation times of the halo CMEs to ~1 AU using empirical CME arrival model developed by Gopalswamy et al. (2001). In this model the CME is assumed to accelerate from the Sun up to ~0.76 AU, after which it is assumed to travel at a constant speed thereafter. Based on a few CME observations, the CME acceleration was expressed as: $a = 2.193 - 0.0054V_{CME}$, where a is the acceleration and V_{CME} is CME speed near the Sun. Based on observations during 49 CME events, Michalek et al. (2004) developed an "improved" expression for this acceleration as: $a = 4.11 - 0.0063V_{CME}$. By excluding the extremely slow and fast events from their database, a third expression was developed: $a = 3.35 - 0.0074V_{CME}$. In this present work, we will test above three acceleration expressions and estimate the probable CME arrival times to determine whether we can now predict the arrival times of ICMEs at Earth during extremely active solar intervals. These three propagation models are hereafter referred to as Mod1, Mod2 and Mod3, respectively. The CME list and near-Sun CME parameters are collected from the SOHO/LASCO CME catalogue (https://cdaw.gsfc.nasa.gov/CME_list/index.html).

Interplanetary discontinuities

To study the interplanetary characteristics of the space weather events, the solar wind plasma and IMFs are obtained from the NASA WIND spacecraft (https://wind.gsfc.nasa.gov/) stationed in a halo orbit around the L1 Lagrange point, ~238 Earth radii upstream of the Earth. The IMFs will be displayed in geocentric solar magnetospheric (GSM) coordinates, where the x-axis is directed towards the Sun, the y-axis is in the $\Omega \times \hat{x}/|\Omega \times \hat{x}|$ direction where Ω is aligned with the magnetic south pole axis. The z-axis completes a right-hand system.

To identify the nature of an interplanetary discontinuity, we estimated the normal (θ_{Bn}) to the discontinuity relative to the upstream IMF using the Abraham-Shrauner (1972) mixed-mode

method. To determine if the discontinuity is a fast shock or instead a submagnetosonic wave, the Rankine-Hugoniot conservation equations are applied to high-time resolution (~3 sec) upstream and downstream plasmas (Smith, 1985; Tsurutani & Lin, 1985; Tsurutani et al., 2011). The magnetosonic Mach number (MMN) is estimated by comparing the discontinuity speed to the calculated upstream magnetosonic wave speed.

Apart from the shocks and waves, there is another major and sometimes important discontinuity detected in the interplanetary data. This is called heliospheric current sheet (HCS). HCSs can be identified by simultaneous polarity reversals of the IMF Bx and By components (Ness & Wilcox, 1964; Smith et al., 1978; Tsurutani et al., 1995). A high plasma density region adjacent to the HCS has been named the heliospheric plasma sheet (HPS: Winterhalter et al., 1994). Both HCSs and HPSs are found to play space weather roles in this active interval of study.

ICMEs, HSSs and CIRs

CMEs propagating through interplanetary space are known as ICMEs. This is because not all 3 parts of a CME, namely MC, coronal loop and a filament (Illing & Hundhausen, 1986), are detected at 1 AU. Furthermore, the parts of the CME may be distorted or even rotated as they propagate from the Sun to 1 AU. "Fast" ICMEs, those propagating faster than the local upstream magnetosonic speed, result in the formation of interplanetary shocks antisunward of the CMEs. The shocks create downstream (sunward) interplanetary sheaths identified by compressed, heated and turbulent solar wind plasma and large amplitude magnetic field variations (Kennel et al., 1985; Tsurutani & Lin, 1985; Tsurutani et al., 1988). A subset of ICMEs are identified as MCs, with smooth magnetic field rotations and enhanced magnitudes, coupled with reduced proton temperatures and low plasma βs (Burlaga et al., 1981; Klein & Burlaga, 1982).

The solar wind HSSs emanating from CHs (Burlaga et al., 1978; Sheeley & Harvey, 1981) are identified in this paper with lower cutoff of speeds Vsw > 550 km s^{-1}. The CIRs are identified in the interaction region between HSSs and slow (Vsw ~300-400 km s^{-1}) streams as characterized by high plasma densities, temperatures and magnetic field amplitudes as mentioned previously.

Magnetic storms, SSSs and GICs

The symmetric ring current SYM-H indices (Sugiura, 1964; Wanliss & Showalter, 2006) are obtained from the World Data Center for Geomagnetism, Kyoto, Japan (http://wdc.kugi.kyoto-u.ac.jp/). These indices will be used to identify and study geomagnetic storms. The auroral SME and SML indices (Gjerloev, 2009) are based on ~300 ground-based magnetometer data taken from the SuperMAG network (http://supermag.jhuapl.edu/). The indices indicate auroral activity levels. Supersubstorms are defined as those events with peak SML < -2500 nT (Tsurutani et al., 2015; Hajra et al., 2016). The geomagnetically induced currents (GICs) measured in the natural gas pipeline near Mäntsälä, Finland (geographic: 60.6°N, 25.2°E) (Pulkkinen et al., 2001; Viljanen et al., 2006) are available from the Space and Earth Observation Centre of the Finnish Meteorological Institute (http://space.fmi.fi/). These GIC data are used in this study.

Relativistic electrons

To study the outer zone radiation belt dynamics during this month-long space weather interval, relativistic electron variations of the 2.00-7.15 MeV electron fluxes measured by the Relativistic Electron-Proton Telescope (REPT) instrument onboard the NASA Van Allen Probes (VAPs: Kessel et al., 2013; Mauk et al., 2013) are used. The data can be obtained at http://vanallenprobes.jhuapl.edu/index.php. The > 0.8 MeV and > 2.0 MeV electrons measured by the Energetic Proton, Electron, and Alpha Detector (EPEAD) instrument onboard GOES 15 stationed at geosynchronous (L ~6.6) orbit will also be used in this part of the study (https://www.goes.noaa.gov/).

3. Results

3.1. Major solar flares during September 2017

Figure 1 shows the X-ray fluences at 1-8 Å and 0.5-4 Å wavelength ranges from GOES/SXI from 1 through 30 September 2017. A large number of solar flares were recorded, among which 4 were X-class and 27 were M-class flares. This extreme solar flare activity was attributed to the extremely rapid development and increasing complexity of active region AR12673 that occurred during the AR passage over the Sun's western half of the visible disk (e.g., Chertok et al., 2018; Seaton & Darnel, 2018; Augusto et al., 2019).

The most powerful flares during the interval of study can be noted to occur during the first 10 days of the month. The major (> 10^{-4} W m^{-2}) X-flare (XFlare) details are listed in Table 1.

XFlare1 erupted at ~08:57 UT on 6 September and continued until ~09:17 UT. It attained its peak flux intensity (X2.2 flare) at ~09:10 UT. This flare eruption originated from AR12673 around the equatorial region on the Sun's west limb (S08W33).

XFlare2 erupted at ~11:53 UT on 6 September had a peak flux intensity of X9.3 at ~12:02 UT. It continued until ~12:10 UT. This was the strongest flare of the month as well as being the most intense event of SC 24.

At ~14:20 UT on 7 September XFlare3 occurred when AR12673 moved closer to the western limb (S11W49). The flare attained its peak flux at ~14:36 UT and ended at ~14:55 UT.

XFlare4 had an intensity of X8.2. It erupted at ~15:35 UT on 10 September from AR12673 when it was in the extreme western limb (S14W74). The flare attained its peak flux at ~16:06 UT and ended at ~16:31 UT.

3.2. CME propagation

During September 2017 the SOHO/LASCO coronagraph detected ~68 CMEs which were associated with AR12673. Four of the CMEs were halo events directed towards the Earth. In Table 2 we have listed the halo CMEs (hCMEs) and their estimated speeds near the Sun. The estimated arrival times based on empirical models (Mod1, Mod2, Mod3) are also shown and compared with the actual observations of the interplanetary counterparts/fast shocks.

hCME1 erupted at ~20:36 UT on 4 September was associated with a M5.5 flare that started at ~20:28 UT, attained peak intensity at ~20:33 UT and ended at ~20:37 UT (not shown). For this halo CME, an interplanetary fast forward shock was detected at ~1 AU by the WIND spacecraft

at ~23:02 UT on 6 September. The three models predicted earlier arrivals of the hCME1 by ~11 h, 13 h and ~3 h, respectively, compared to the actual shock detection.

The best predictions were found for the hCME2 that erupted at ~12:24 UT on 6 September in association with the X9.3-class flare (XFlare2, Table 1). The models Mod1, Mod2 and Mod3 predicted the CME arrival times at 1 AU at ~22:48 UT on 7 September, at ~21:36 UT on 7 September and at ~04:34 UT on 8 September, respectively. The actual fast forward shock detection by the WIND spacecraft was at ~22:19 UT on 7 September. Thus, the predicted arrival times are delayed by ~24 min by Mod1, occurs ~36 min earlier in Mod2, and is ~6 h 18 min delayed by Mod3. One could say that all three predictions were reasonably accurate for this CME event. Since the CME prediction is not the shock time prediction, these results are quite accurate.

hCME3 erupted at ~16:00 UT on 10 September near Sun arrived at ~1 AU (WIND) at ~19:12 UT on 12 September. This CME was associated with the second strongest (X8.2) flare of September (XFlare4, Table 1). However, the three models predicted > 35 h earlier arrivals of the CME. It may be mentioned that the near-Sun CME speed was exceptionally high (3163 km s^{-1}) for this event. Any possible error in speed measurement might be associated with this large prediction error.

For the hCME4 event launched from the Sun at ~12:00 UT on 17 September, no C-class or higher flare was detected by GOES/SXI. The models Mod1, Mod2 and Mod3 predicted arrivals of the CME at 1 AU at ~04:19 UT, ~02:10 UT and ~13:12 UT on 19 September, respectively. However, no significant interplanetary signature was detected in the WIND interplanetary data. Thus, although this was a halo CME, deflection or some other effect must have happened so that it missed the Earth.

From the above discussion, it may be noted that the solar flares XFlare2 and XFlare4 were associated with the halo CMEs: hCME2 and hCME3, respectively. However, no halo CMEs were erupted in association with XFlare1 and XFlare3. XFlare1 was found to be associated with a CME which erupted at ~09:48 UT on 6 September with a central position angle (CPA) of 245° and an apparent angular width of ~80°. The CME with a liner speed of ~391 km s^{-1} near the Sun slowed down at a rate of ~-13.8 m s^{-2} within the SOHO/LASCO field of view. On the other hand, XFlare3 was associated with a CME which erupted at ~15:12 UT on 7 September. The CME, with an initial linear speed of ~433 km s^{-1} near the Sun, slowed down at a rate of ~-9.9 m s^{-2}. None of these two CMEs arrived at the Earth as far as the authors could determine.

3.3. Interplanetary discontinuities and their geomagnetic effects

Figure 2 shows an overview plot of the solar wind plasma, IMFs, and geomagnetic variations during September 2017. The major interplanetary events are marked. Eleven major interplanetary discontinuities are identified. Among them, 6 were fast forward shocks (indicated by red solid vertical lines), 2 were reverse waves (red dashed vertical lines), and 3 were HCSs (green solid vertical lines). The interplanetary characteristics and associated geomagnetic impacts of the discontinuities are listed in Table 3. These will be discussed below.

Fast forward shocks

During 6 of the 11 discontinuities, the solar wind speed Vsw, plasma density Nsw, ram pressure Psw, temperature Tsw, and IMF amplitude Bo all increased abruptly from upstream (antisunward) to downstream (sunward) of the discontinuities. These were identified as fast (magnetosonic) shocks propagating in the antisolar (forward) direction. These are marked sequentially as FS1 to FS6 in Figure 2 and Table 3. The shocks propagate with speeds larger than the upstream magnetosonic speed, thus they all have magnetosonic Mach numbers (MMNs) greater than 1.0 (by definition). Fast forward shocks have downstream density compressions that are approximately equal to the Mach number for low Mach number shocks (MMN < 4) and maximum compression of ~4 for high Mach number shocks (MMN > 4) (Kennel et al., 1985; Tsurutani et al., 2011). Thus, when the shock/sheath impacts the Earth's magnetosphere, a strong compression takes place which can lead to several types of different magnetospheric space weather effects. Among 6 fast forward magnetosonic shocks detected by the WIND spacecraft, 3 (FS1, FS2 and FS3) were associated with Earth-directed halo CMEs, and 3 (FS4, FS5 and FS6) were associated with CIRs followed by HSSs.

FS1 occurred at ~23:02 UT on 6 September was associated with hCME1 which erupted on 4 September (Table 2). The shock was found to propagate at ~5.8 times of the magnetosonic speed in the perpendicular direction (θ_{Bn} ~90°) to the ambient IMF. This unusual purely perpendicular shock, with a ram pressure Psw increase of a factor of ~7, caused a major sudden impulse (SI^+) of ~+56 nT. The SI^+ occurred at ~00:46 UT on 7 September and is noted in the SYM-H index panel.

FS2 detected at ~22:19 UT on 7 September was associated with hCME2 on 6 September (Table 2). The shock was estimated to be propagating at ~6.7 times of the magnetosonic speed at an angle of ~48° relative to the IMF, and was characterized by a factor of ~5 increase in Psw leading to a SI^+ of ~+20 nT at ~23:03 UT. It also triggered an intense auroral supersubstorm (SSS1) (Tsurutani et al., 2015) with peak SME and SML intensities of 4464 nT and -3712 nT, respectively, at ~00:24 UT on 8 September. This supersubstorm will be discussed in more detail later in Section 3.6.

FS3 occurred at ~19:12 UT on 12 September. FS3 was associated with the hCME3 on 10 September (Table 2). The shock was found to be quasi-parallel in nature with θ_{Bn} ~19°, moving with a speed ~4 times the upstream magnetosonic speed. Even though the shock was quasi-parallel, it was characterized by a Psw jump by a factor of ~8 and caused a SI^+ of ~+27 nT at ~20:09 UT. FS3 triggered a moderate substorm with SME and SML peaks of 1366 nT and -1071 nT, respectively. These substorm peaks occurred at ~21:04 UT on 12 September.

The fast forward shocks FS4, FS5 and FS6 (Figure 2 and Table 3) were detected at ~00:00 UT on 14 September, at ~10:05 UT on 14 September, and at ~22:48 UT on 26 September, respectively. All three shocks occurred at the leading (antisolar) edges of the CIRs (to be discussed in more detail later in Section 3.5).

FS4 was determined to be quasi-parallel, moving at ~4.3 times of the upstream magnetosonic speed at an angle ~9° relative to the ambient IMF. It was characterized by a factor of ~4 ram pressure Psw jump resulting in a SI^+ ~+14 nT at ~01:31 UT on 14 September.

FS5 was quasi-perpendicular (θ_{Bn} ~84°) in nature and was a Mach ~1.7 shock. A ramp pressure Psw jump by a factor of ~4.5 led to a SI^+ ~+28 nT which occurred at ~12:12 UT on 14 September.

FS6 was determined to propagate at ~2.7 times of the upstream magnetosonic speed at an angle of ~34° relative to the ambient IMF. A SI^+ of ~+14 nT was induced at ~23:55 UT on 26 September by a ram pressure Psw jump of ~3 across this shock.

FS4, FS5 and FS6 did not trigger substorms. This may have to do with precursor interplanetary magnetic fields being mostly northward.

Reverse waves

Two of the 11 discontinuities were characterized by Vsw increases with the other parameters (Nsw, Psw, Tsw, Bo) simultaneously decreasing with time. In addition, these were determined to be moving at submagnetosonic speeds, indicating that they were not shocks, but reverse waves (RWs). By "reverse" we mean that the waves were propagating towards the Sun but because the solar wind speed is higher than the speed of the waves, the waves were convected in the antisolar direction. These two waves are marked by RW1 and RW2 in Figure 2 and Table 3.

RW1 at ~18:29 UT on 14 September was determined to have speed ~84% of the upstream (sunward) magnetosonic speed. The angle of propagation was ~71° relative to the ambient IMF. The ram pressure Psw decreased with time across RW1 by a factor of ~1/7. Thus, when RW1 impacted the Earth's magnetosphere, it caused a decompression of the magnetosphere, opposite to what happens when a forward shock/wave impacts the magnetosphere. RW1 caused a negative sudden impulse (SI^-) of ~-23 nT at ~21:08 UT on 14 September. RW1 also caused a substorm recovery as seen from an increase in SML index from a value of ~-584 nT at ~18:40 UT to ~-133 nT at ~19:40 UT.

RW2 occurred at ~08:38 UT on 28 September and had a speed ~71% of the upstream magnetosonic speed. It was propagating oblique to the ambient magnetic field at an angle of ~87°. The ram pressure Psw decreased by a factor of ~1/3 across the RW2. It caused a SI^- of ~-14 nT at ~09:37 UT on 28 September. RW2 was associated with a substorm recovery phase as seen in SML decrease from ~-813 nT at ~09:31 UT to ~-198 nT at ~10:04 UT.

HCSs and HPSs

The HCS crossings represent tangential discontinuities where the IMF Bx and By exhibit simultaneous polarity/sign reversals. Three HCSs detected during this study are marked as HCS1, HCS2 and HCS3 in Figure 2 and Table 3.

HCS1 occurred at ~14:10 UT on 14 September. It was characterized by simultaneous positive-to-negative Bx and negative-to-positive By polarity reversals. By convention (Ness & Wilcox, 1964), magnetic fields pointed outward from the Sun have a "positive" polarity. A peak plasma density of ~40 cm^{-3} was associated with HPS1. It triggered a moderate substorm with peak SML intensity of -766 nT and SME intensity of 1171 nT at ~15:41 UT.

HCS2 occurred at ~21:22 UT 24 September, characterized by negative-to-positive Bx and a positive-to-negative By polarity reversals. HPS2 had a peak plasma density of ~36 cm^{-3}. No substorm was triggered by HPS2.

HCS3 occurring at ~05:17 UT on September 27 exhibited a simultaneous positive-to-negative Bx and a negative-to-positive By polarity reversal. The associated HPS3 had a peak density of

~54 cm^{-3}. It triggered a substorm with peak SML intensity of -614 nT and SME intensity of 883 nT at ~07:39 UT.

In addition to the interplanetary discontinuities described above, the interplanetary space during September 2017 was characterized by interplanetary sheaths, ICMEs, and CIRs. The detailed case-by-case analyses of the interplanetary events, their characteristics and geomagnetic impacts will be presented next in the Sections 3.4 – 3.7.

3.4. Interplanetary sheaths, ICMEs and their geomagnetic effects

In this section, we study the interplanetary sheaths and MCs identified during September 2017, and their geomagnetic impacts. The event durations and their major impacts are listed in Table 4.

Interplanetary events during 6 – 11 September

Figure 3 shows interplanetary events and associated geomagnetic impacts during 6 – 11 September 2017. Two interplanetary sheaths were detected during this period. Sheath1 extended from FS1 at ~23:02 UT on 6 September to FS2 at ~22:19 UT on 7 September. Sheath2 followed FS2 at ~22:19 UT on 7 September to ~11:02 UT on 8 September (Table 4). The sheaths are marked by green horizontal bars on the top of Figure 3. These were characterized by large IMF Bz fluctuations with peak southward Bz components of ~-11 nT at 05:51 UT and ~-31 nT at ~23:02 UT on 7 September, respectively. Sheath1 was comparatively less geoeffective, associated SYM-H peak was only -15 nT. A moderate substorm with SME and SML peak intensities of 1417 nT and -1097 nT, respectively at ~09:05 UT was recorded during Sheath1. The southward Bz associated with Sheath2 caused a sharp decrease in SYM-H index with peak magnetic storm intensity of -146 nT at ~01:10 UT on 8 September (intense magnetic storm, IMS1: Gonzalez et al., 1994). The storm main phase was associated with a long-duration (~3.2 h) southward component of the Sheath2 IMF. The SSS1 in this magnetic storm main phase (mentioned previously) was triggered by FS2, while the Sheath2 southward field appears to have acted as the energy source for the SSS1.

Sheath2 was followed by a MC, which occurred from ~11:02 UT on 8 September through ~00:43 UT on 11 September (Table 4). This is marked by a red horizontal bar at the top of Figure 3. The MC is identified by low plasma β (~2×10^{-2}), low Tsw (~4×10^{4} K), a negative-to-positive rotation in Bx, and a south-to-zero Bz configuration. The initial southward IMF component lasted ~3.7 h with peak negative Bz intensity of -17 nT at ~11:22 UT on 8 September. This southward Bz was responsible for development of the main phase of the second intense storm (IMS2). This had a peak SYM-H intensity of -115 nT at 13:56 UT on 8 September. This interval was also associated with an SSS (SSS2) with SME and SML peak intensities of 4330 nT and -2642 nT, respectively. The peak SSS2 intensity occurred at ~13:08 UT on 8 September. The SSS2 will be discussed latter in more detail in Section 3.6.

Interplanetary events during 12 – 13 September

Interplanetary events and resultant geomagnetic activity during 12 – 13 September are shown in Figure 4. The interplanetary variations following FS3 (associated with hCME3) indicate some unclear events. The interval from ~19:12 UT on 12 September to ~03:22 UT on 13 September is characterized by large IMF fluctuations with southward Bz components lasting for ~25 min, ~28 min, ~26 min and ~43 min durations with peak intensities of ~-8 nT, ~-8 nT,

~-12 nT and ~-11 nT, respectively. This possibly may be indicative of an interplanetary sheath (marked as Sheath3, Table 4). This will be further discussed in the discussion section. The Sheath3 led to a moderate magnetic storm (MMS1) with SYM-H peak intensity of -65 nT at ~00:12 UT on 13 September.

Two auroral substorms were detected during this interval. One substorm had peak SME and SML indices of 1366 nT and -1071 nT, respectively, at ~21:04 UT, and the other had peak SME and SML intensities of ~1856 nT and ~-1541 nT, respectively at ~23:57 UT on 12 September.

Sheath4 occurred between FS4 and FS5, from ~00:00 UT to ~10:05 UT on 14 September. This had only weak IMF Bz southward component of ~-4 nT. While no magnetic storm was detected during this interval, auroral activity had peak SME and SML intensities of 389 nT and -306 nT at ~05:29 UT on 14 September.

3.5. Interplanetary HSSs, CIRs and their geomagnetic effects

From the variations of solar wind plasma speed Vsw, 3 HSSs were identified (see Figure 2). CIRs were identified as the compressed plasma and magnetic fields in the interaction regions between low-speed streams and HSSs. It may be noted that the CIR event associated with HSS1 occurred before 1 September, so this was not included in the present analysis. The HSS and CIR event intervals, their Vsw characters and major impacts are listed in Table 5.

HSSs

HSS1 had a peak plasma speed Vsw of ~687 km s^{-1} at ~15:00 UT on 1 September (Table 5). This event extended to approximately the end of 2 September. The SDO/AIA telescope identified a large coronal hole (CH25) on 28 August as the source of this HSS (not shown). Coronal hole CH25 had a positive magnetic polarity (defined as the magnetic field pointing away from the Sun) and extended from the solar north pole down to ~+5° latitude around ~180° Carrington longitude. No magnetic storm was recorded in SYM-H (the peak SYM-H was -28 nT). Discrete multiple southward components (~-5 nT) of an Alfvén wave train embedded within the HSS1 proper resulted in intense auroral activity, with peak SME and SML intensities of ~1588 nT and ~-1439 nT, respectively. However, this was not an "ideal" high-intensity (SME peak > 1000 nT), long-duration (≥ 2 days), continuous (SME never dropping below 200 nT for > 2 h at a time) auroral electrojet activity (HILDCAA) event defined by Tsurutani & Gonzalez (1987). Although there was a peak SME value of > 1000 nT and the event lasted for > 2 days, the SME decreased below 200 nT for > 2 h several times within the interval.

HSS2 emanated from a coronal hole (CH30) with positive magnetic polarity, extending from the solar north pole down to ~+15° latitude with a Carrington longitude extent of ~80° to ~240°, identified on 14 September. HSS2 had a peak Vsw of ~743 km s^{-1} at ~06:36 UT on 15 September (Table 5). It lasted approximately to the end of 18 September. HSS2 was associated with long-duration IMF Bz fluctuations (peak southward Bz ~-6.6 nT) indicating an Alfvén wave train leading to intense auroral activity as observed in peak SME (~1749 nT) and peak SML (-1423 nT) indices. However, this was again not an "ideal" HILDCAA event. The SME decreased below 200 nT for > 2 h several times. The SYM-H peak intensity was -44 nT, registering no geomatic storm.

HSS3 emanated from a positive magnetic field coronal hole (CH32) on 26 September (extending from north pole of the Sun down to ~-10° latitude at around ~190° Carrington longitude). This HSS impacted the Earth's magnetosphere from 27 to 29 September (Table 5). It had a peak Vsw of ~721 km s^{-1} at ~11:41 UT on 28 September. The HSS3 proper was characterized by intense auroral activity (peak SME ~2044 nT, SML ~-949 nT) associated with Alfvén wave IMF Bz southward fields (peak ~-4 nT). However, HSS3 did not lead to a magnetic storm (SYM-H peak = -43 nT).

14 September CIR (CIR1)

Figure 5 shows the interplanetary events during 13 – 19 September and associated geomagnetic impacts. Following Sheath4, a CIR was identified from ~10:05 UT to ~18:29 UT on 14 September (CIR1). This was characterized by a plasma density (Nsw) enhancement from ~6 to ~56 cm^{-3}, and an IMF Bo enhancement from ~2 to ~22 nT. The leading and trailing edges of the CIR1 were characterized by the fast forward magnetosonic shock FS5 and reverse wave RW1, respectively (Table 3). In addition, a tangential discontinuity HCS1 characterized the complex CIR1 event.

CIR1 did not cause a magnetic storm (SYM-H peak -19 nT). This was presumably because of the short-duration IMF southward components inside the CIR1. For example, two intervals of southward IMFs were detected with durations of ~38 min and ~56 min and peak Bz of ~-19 nT and -16 nT, respectively. While intensities of southward IMF were high, short durations indicate lesser amount of magnetospheric energy input which is not sufficient for a magnetic storm (Gonzalez et al., 1994).

26 – 28 September CIR (CIR2)

The interval from 23 to 30 September is illustrated in Figure 6. A CIR was identified from ~22:48 UT on 26 September to ~08:38 UT on 28 September (CIR2). The plasma density Nsw increased from ~12 to ~59 cm^{-3}. The IMF Bo increased from ~3 to ~17 nT. The fast forward shock FS6 and reverse wave RW2 were located at the leading and trailing edges of the CIR2, respectively (Table 3). The HCS3 was detected inside CIR2.

CIR2 caused a moderate intensity magnetic storm (MMS2). The storm was characterized by a gradual, multi-step main phase development with SYM-H peak intensity of -74 nT at ~05:57 UT on 28 September. The southward component of Alfvénic IMF was responsible for this moderate storm. For example, southward IMF intervals of ~2 h, ~3.5 h, ~1.4 h and ~1.3 h were recorded with peak Bz of ~-15.4 nT, ~-11.3 nT, ~-10.5 nT and ~-9.5 nT, respectively inside the CIR2. During the storm main phase, peak SME and SML intensities were 2683 nT and -1813 nT, respectively.

3.6. SSSs and GIC effects

Two SSSs (SML < -2500 nT) were detected during September 2017. These occurred on 7-8 September (Figure 3). They were found to induce strong GICs in the Finnish natural gas pipeline. The SSS characters and associated GIC recordings are summarized in Table 6.

SSS1 started at ~22:19 UT on 7 September preceded by an IMF southward turning at ~19:30 UT. The SSS energy loading was associated with Sheath1 southward field with peak Bz component of ~-31 nT at ~23:02 UT on 7 September. It was triggered by the fast forward shock

548 FS2 (Table 3). The SSS attained its peak SML intensity of -3712 nT at ~00:24 UT and ended
549 at ~02:51 UT on 8 September. It had a total duration of ~4 h 32 min. This SSS occurred in the
550 main phase of an intense magnetic storm (IMS1) with SYM-H peak intensity of -146 nT, the
551 SML peak occurring ~46 min earlier than the SYM-H peak (see Section 3.4). The SSS1
552 recovery phase was associated with very intense GICs at the Finland station which at the time
553 was in local postmidnight. The GIC had a peak eastward intensity of ~28 A at ~03:31 local
554 time (LT = UT + 3 h).
555
556 SSS2 started at ~11:34 UT and ended at ~15:42 UT on 8 September, with a total duration of
557 ~4 h 8 min. The SSS onset was preceded by an IMF southward turning at ~10:26 UT as a part
558 of the MC1 and was triggered by a high ram pressure Psw region. This Psw region occurred
559 from ~08:13 UT to ~11:14 UT with a peak Psw of ~8.5 nPa. The SSS was characterized by a
560 peak SML intensity of -2642 nT at ~13:08 UT. This was preceded by an IMF precursor Bz
561 peak of -17 nT at ~11:22 UT. SSS2 was also detected in the intense magnetic storm main phase
562 which had a SYM-H intensity of -115 nT (IMS2). The SSS SML peak occurred ~48 min earlier
563 than the SYM-H peak (Section 3.4). Large amplitude GICs occurred during the SSS2 recovery
564 phase, with peak (eastward) component of ~30 A at ~20:55 LT.
565
566 **3.7. Outer zone radiation belt variation**
567
568 Responses of the outer zone radiation belt to the complex and multiple space weather events
569 during 1 through 30 September are shown in Figure 7. Varying interplanetary and
570 magnetospheric space weather events can be related to changes in the relativistic electron
571 fluxes.
572
573 ***Effects of interplanetary discontinuities on relativistic electron fluxes***
574
575 Figure 7 shows that at the GOES 15 geosynchronous orbit, the fast forward shock FS1 led to a
576 relativistic > 0.8 MeV and > 2.0 MeV electron flux decrease by ~1 order of magnitude followed
577 by a further ~1 order of magnitude decrease caused by the following fast shock FS2. The
578 combination of the two shocks resulted in a net flux decrease of ~2 orders of magnitude from
579 ~990×10^2 to ~450 cm^{-2} sr^{-1} s^{-1} for > 0.8 MeV electrons, and from ~90×10^2 to ~90 cm^{-2} sr^{-1} s^{-1}
580 for > 2.0 MeV electrons. This occurred during the main phase of the intense storms of 7 – 8
581 September. The VAP L-shell observations show that the entire outer radiation belt was flux-
582 depleted during this period. The flux depletions were most prominent around L ~4-5 for the 2-
583 4.50 MeV electrons.
584
585 The combination of FS3, FS4 and FS5 (at the leading edge of the CIR1) depleted the outer
586 zone radiation belt during 13 – 14 September. At the geosynchronous orbit the net flux decrease
587 was ~2 orders of magnitude. From the VAPs L-shell flux observations, clear energy
588 dependence can be noted. The strongest flux depletions were recorded at L > 5 for 2-2.30 MeV
589 electrons, at L > 4.5 for 2.85 MeV electrons, and at L > 4 for ≥ 3.60 MeV electrons. No
590 prominent magnetospheric impacts of the HPS1 and RW1 were apparent.
591
592 The outer zone (L > 4) magnetosphere relativistic electron belt was strongly depleted by the
593 solar wind ram pressure pulses of HPS2, FS6 and HPS3 during 25 – 28 September. No
594 prominent impacts were recorded owing to RW2.
595
596 ***Effects of MC on relativistic electron fluxes***
597

The MC and the magnetic storm it induced (IMS1) was associated with large relativistic electron flux increases compared to pre-shock flux values. This increase was mainly for L < 5. Presumably the storm time convection electric field injected the energetic ~30 to 300 keV electrons deep into the magnetosphere with further particle energization by chorus wave interactions. Flux enhancements by > 2 orders of magnitude were noted around L ~3-4 associated with the magnetic storm discussed in Section 3.4. Most interestingly, the low flux density slot region (2 < L < 2.5) separating the inner (L < 2) and outer (L > 2.5) radiation belts moved inward. The large amplitude flux enhancement during the storm recovery phase is interesting. This was characterized by intense auroral SME/SML substorm activity preceded by SSS2. Thus, this portion is most likely acceleration by chorus wave interactions.

Effects of HSSs on relativistic electron fluxes

HSS intervals are found to be characterized by IMF Alfvén wave trains and intense auroral SME/SML activities. The chorus wave generation by the temperature anisotropic ~10-100 keV electron injections are believed to accelerate the ~100 keV electrons to ~MeV energies. It appears that HSS2 and HSS3 did indeed repopulated the radiation belt with > 0.8-7.15 MeV electrons. The largest flux enhancements were recorded around L ~4-5.5. It may be recollected that peak flux enhancements due to the MC were deeper into the magnetosphere, at L ~3-4. For the 2.85-7.15 MeV electrons, two separated belts can be identified during 16 – 27 September: a radiation belt enhanced by the MC around L ~3-3.5 and an enhanced belt due to HSS2 around L ~4-5.

4. Discussion

September 2017 was an interesting period for complex and multiple space weather events occurring during a descending-to-minimum solar cycle phase. Extremely rapid development and increasing complexity of AR12673 resulted in eruptions of numerous class-C and above solar flares and CMEs. Multiple well-developed and extended CHs emitting HSSs contributed to space weather complexity during this period.

Solar Flares and CMEs

Out of four X-class, twenty-seven M-class and numerous C-class solar flares that occurred from AR12673 on the western limb, three were related to halo CMEs. Among the three flares causing halo CMEs, one was M-class (M5.5) and two were X-class (X9.3 and X8.2) flares. No C-class or above flare was associated with one halo CME. This may have been associated with a disappearing filament (Tang et al., 1989; Zhou et al., 2003; Lepri & Zurbuchen, 2010). On the other hand, two X-class (X2.2 and X1.3) flares did not have associated halo CMEs. These solar results are consistent with previous reports (e.g., Chertok et al., 2018; Redmon et al., 2018; Yan et al., 2018; Zou et al., 2019).

Among the four halo CMEs detected during this period, three arrived at 1 AU, as detected by fast forward shocks followed by sheaths and/or MC. However, no significant interplanetary signature was recorded at 1 AU during one halo CME. Deflections away from the straight line propagation during active interval or some other effects are suggested to happen so that it missed the Earth. We estimated the propagation times of halo CMEs from the Sun to Earth based on near-Sun CME speed measurement. We used an empirical CME arrival model (Gopalswamy et al., 2001) employing three different expressions for CME acceleration (Gopalswamy et al., 2001; Michalek et al., 2004) up to ~0.76 AU, after which the CME was

assumed to travel at a constant speed up to ~1 AU. The prediction errors varied from ~24 min to > 35 h with respect to the actual CME signatures detected by the WIND spacecraft (~1 AU). However, any possible error in near-Sun CME speed measurement can cause the above prediction errors. In addition, as previously discussed by Echer et al. (2009), modelling CME propagation delays during solar active intervals is difficult due to the complexity of the interplanetary medium. Codes that work for simple events may not be accurate during periods when multiple CMEs are being launched from the Sun.

Magnetic Storms

There were two intense (peak SYM-H ≤ -100 nT) and two moderate (-100 nT < peak SYM-H ≤ -50 nT) magnetic storms during September 2017. None were at the superstorm level (SYM-H peak ≤ -250 nT). The intense storms (with peak SYM-H of -146 nT and -115 nT) occurred consecutively on 8 September. The first storm was caused by southward IMF Bz fields in the Sheath2. The second storm was caused by southward IMF Bz fields in the MC. A moderate storm (with peak SYM-H of -65 nT) was caused by another sheath (Sheath3) on 13 September. These three events were related to halo CMEs: hCME1, hCME2 and hCME3, respectively. As mentioned previously, Sheath3 represented an unclear event. This was not followed by a MC. We explored the possibility of this being a filament (Tang et al., 1989; Zhou et al., 2003; Lepri & Zurbuchen, 2010; Kozyra et al., 2014). However, filaments inside ICMEs are reported (e.g., Lepri & Zurbuchen, 2010) to be low-temperature. The present event (Sheath3) was determined to be a sheath due to its high temperature in addition to compressed and turbulent plasma and IMF features. For hCME4 no clear interplanetary signature and geomagnetic impact were identified at the Earth. The second moderate storm (peak SYM-H of -74 nT) on 27-28 September was associated with the CIR2 event. CIR1 on 14 September did not cause any magnetic storm.

No magnetic storms were caused by three HSS events detected in this study. However, they led to intense (peak SME ~1588 nT, ~1749 nT, ~2044 nT) and continuous auroral activity for several days. While long-duration (> 3 h), intense southward IMFs in the sheaths and the MC led to intense magnetic storms, short-duration (< 1 h), sporadic southward components within the CIRs and HSSs caused only moderate magnetic storms with peak SYM-H > -100 nT. However, as expected, the short duration IMF Bz components caused intense, long-duration auroral activity. These are consistent with present understanding of geoeffectiveness of interplanetary events like ICMEs, CIRs and HSSs (e.g., Tsurutani & Gonzalez, 1987; Tsurutani et al., 1988, 1995, 2006; Gonzalez et al., 1994; Zhang et al., 2007; Echer et al., 2008; Hajra et al., 2014; Meng et al., 2019).

Studies on the intense storm of 8 September were reported previously (e.g., Berdermann et al., 2018; Clilverd et al., 2018; Shen et al., 2018; Augusto et al., 2019). The storm was attributed to the combined interplanetary shock-ICME events, which corroborates with the present analysis.

Sudden impulses, substorm triggers and recoveries

There were six FSs with Mach numbers ranging from ~1.7 to ~6.7 and with planar normal oriented at ~9° to ~90° relative to the ambient upstream magnetic field direction. All FSs caused SI^+s ranging from ~+14 nT to ~+56 nT. Two of the FSs triggered substorms. There were three HCSs characterized by simultaneous IMF Bx, By polarity changes. The associated HPS pressure pulses triggered substorms. Substorm triggering by FS/HPS pressure pulses was

noted to be preceded by IMF southward turning indicating magnetospheric energy preloading. Two quasi-perpendicular RWs moving at submagnetosonic speeds were detected. Both initiated substorm recoveries.

Supersubstorms and GIC effects

Two SSSs were detected during September 2017. These were preceded (~2.8 h and ~1.1 h) by precursor southward IMFs. SSSs were triggered by solar wind ram pressure pulses. Analysis of current measurements in Finnish natural gas pipeline indicates that the SSSs led to large GICs in the local dusk and postmidnight sectors. The GICs are known to be related to large dB/dt variations (e.g., Pirjola, 2000; Viljanen et al., 2001; Boteler, 2003). It may be noted that there are previous reports of ground electrical anomalies and/or power outages occurring during magnetic storms (e.g., Loomis, 1861; Allen et al., 1989; Lanzerotti, 1992). Magnetic storm ring current intensifications are unlikely to directly impact ground power grid systems.

Outer zone relativistic electrons

It was shown that substantial outer zone magnetospheric relativistic electron fluxes decreased when interplanetary FSs and HCSs/HPSs impinged on the magnetosphere. Tsurutani et al. (2016) showed that HPSs caused non-storm relativistic electron flux decreases. Hajra & Tsurutani (2018b) showed that FSs can also cause flux decreases. The scenario is that solar wind pressure pulses cause the generation of coherent electromagnetic ion cyclotron (EMIC: Cornwall, 1965; Kennel & Petschek, 1966) waves in the dayside magnetosphere. These waves can have parasitic resonant interaction with relativistic electrons, causing their pitch angle scattering and loss to the atmosphere (Thorne & Kennel, 1971; Meredith et al., 2003; Summers et al., 2007; Remya et al., 2015; Tsurutani et al., 2016). However, there is another possibility of a relativistic electron loss mechanism, that of "magnetopause shadowing" where the electrons gradient drift to the magnetopause and are lost into the solar wind (West et al., 1972; Li et al., 1997; Hudson et al., 2014). At this time, it is uncertain which of the two mechanisms dominate. It seems quite likely that both are occurring. It is possible that the dominant effect may vary from case to case. Further research on this topic is needed.

Relativistic electron flux enhancements were recorded during the HSS intervals and the MC associated with the magnetic storm recovery phase. The largest flux enhancements during the HSSs were recorded around L ~4-5.5. However, the peak flux enhancements owing to the MC induced storm convection were deeper into the magnetosphere, at L ~3-4. In addition, during the MC event, the slot region separating the inner ($L < 2$) and outer ($L > 2.5$) radiation belts occurred at lower L. These results corroborate with previous results (Baker et al., 2014; Kanekal et al., 2015). Tsurutani et al. (2018) have speculated that the electron slot is created by coherent chorus waves propagating into the plasmasphere and interacting with the relativistic electrons. This new mechanism will cause rapid loss of the electrons during the chorus (substorm/storm) event.

5. Summary and Conclusion

We explored the solar, interplanetary and geomagnetic events occurring during September 2017. This interval was in a descending-to-minimum phase of a solar cycle. The main results are summarized below.

1. There were 4 X-class, 27 M-class and a myriad of C-class flares and ~68 CME eruptions from solar active region AR12673. Only 4 halo CMEs were detected, among them 3 reached the Earth, and 1 did not reach the Earth.
2. The two strongest flares (X9.3 and X8.2) of the present study were associated with two halo CMEs. A third halo CME was associated with a M5.5 flare. No solar flare was detected during the fourth halo CME. Thus, a complex relationship between flares and halo CMEs is indicated.
3. Six fast forward magnetosonic shocks (FSs) were detected (Figure 2, Table 3). Half of them were associated with halo CMEs (Table 2) and half were detected at the leading antisolar edges of CIRs. The angle of propagation (θ_{Bn}) of the FSs varied from ~9° to ~90° relative to the ambient IMFs, while their strengths varied from Mach ~1.7 to Mach ~6.7. The induced SI^+ strengths varied between ~+14 nT to ~+56 nT. Two CME FSs triggered substorms. None of the CIR FSs triggered substorms due to a lack of prior southward IMF conditioning. The FS impingements on the magnetosphere led to large MeV electron flux depletions in the Earth's outer radiation belt (L > 4) (Figure 7).
4. Two non-shock reverse waves (RWs) were detected at the trailing edges of the CIRs (Figure 2, Table 3). They were found to be propagating mostly across the magnetic field (θ_{Bn} ~71°-88°) at submagnetosonic (~71-88%) speeds. Both RWs caused negative sudden impulses SI^- ~-14 to -23 nT and both caused the termination of ongoing substorms. There were no reverse shocks detected in this study.
5. Three HCSs were detected (Figure 2, Table 3). HPSs adjacent to two of them triggered moderate intensity substorms. All three high pressure pulses associated with the HPSs led to relativistic electron flux decreases in the outer radiation belt.
6. Southward IMFs associated with an interplanetary sheath and the following MC led to two intense consecutive magnetic storms with peak SYM-H intensities of -146 nT and -115 nT, respectively (Figure 3, Table 4). Two moderate storms with peak SYM-H of -65 nT and -74 nT were caused by southward IMFs associated with another sheath and a CIR event (Figures 4, 6, Tables 4, 5). The MC and the magnetic storm led to relativistic electron flux enhancements (Figure 7). The peak flux enhancements were noted deep within magnetosphere (L ~3-4). In addition, the low flux density slot region (2 < L < 2.5) separating the inner (L < 2) and outer (L > 2.5) radiation belts moved inward.
7. Two SSSs (with peak SML intensities of -3712 nT and -2642 nT) occurred in the main phases of the intense magnetic storms. The SSSs were preceded (~2.8 h and ~1.1 h) by precursor southward IMFs followed by solar wind ram pressure pulse triggering. SSSs were associated with large GICs with peak values of ~28 A and ~30 A recorded in the local (Finland) postmidnight and dusk sectors, respectively (Table 6).
8. Two CIRs were characterized by fast magnetosonic shocks bounding the leading antisolar edges and reverse submagnetosonic waves at the trailing edges (Figures 5, 6, Table 5). Weak and short duration southward IMFs in a CIR led to a moderate magnetic storm with SYM-H peak of -74 nT. However, the other CIR did not lead to a magnetic storm but small ring current activity (SYM-H peak = -28 nT) and high level (peak SME > 1000 nT) auroral zone activity.
9. HSSs were associated with intense auroral activities indicated by the SME and SML indices. However, these were not HILDCAAs in the strict definition. The HSSs did not cause magnetic storms (with SYM-H < -50 nT). The HSSs were associated with relativistic electron flux enhancements prominently around L ~4-5.5 (Figure 7).
10. We estimated the probable halo CME arrival times at ~1 AU from the Sun using an CME arrival model and three different expressions for CME acceleration in the interplanetary space (Table 2). The prediction error varied from ~24 min to > 35 h with

respect to the actual CME signatures detected by the WIND spacecraft. The efficiency of the individual models is found to vary from one event to the other.

In general, we have found nothing particularly unusual in resultant geomagnetic activity in this solar minimum interval than what occurs during solar maximum. All of the basic known solar wind effects on geomagnetic activity can be applied. Perhaps the occurrence of simultaneous HSSs is one small complexity. However, the addition of HSSs only led to auroral zone HILDCAA-like activity and the acceleration of magnetospheric relativistic electron fluxes. The formation of the AR in this solar cycle minimum phase is the source for the halo CMEs and potential magnetic storms. Thus, it will be the goal of the solar physicists to tell us when ARs occur during this phase of the solar cycle so that magnetic superstorms may occur in the future.

Acknowledgements. The work of R. H. is funded by the Science & Engineering Research Board (SERB), a statutory body of the Department of Science & Technology (DST), Government of India through Ramanujan Fellowship at NARL. Portions of this research were done at the Jet Propulsion Laboratory, California Institute of Technology, under contract with NASA. G. S. L. thanks the Indian National Science Academy, New Delhi for the support under INSA-Honorary Scientist Scheme. The solar X-ray fluences measured by the GOES/SXI are collected from: https://www.goes.noaa.gov/. The SOHO/LASCO CME information are available at: https://sohowww.nascom.nasa.gov/. The SDO/AIA CH images are obtained from: https://sdo.gsfc.nasa.gov/. The solar wind plasma and IMFs at L1 are obtained from the NASA WIND spacecraft available at: https://wind.gsfc.nasa.gov/. The symmetric ring current SYM-H indices are obtained from the World Data Center for Geomagnetism, Kyoto, Japan at: http://wdc.kugi.kyoto-u.ac.jp/. The auroral SME and SML indices are taken from the SuperMAG website: http://supermag.jhuapl.edu/. The GICs measured in the natural gas pipeline near Mäntsälä, Finland are available from the Space and Earth Observation Centre of the Finnish Meteorological Institute at: http://space.fmi.fi/. The NASA Van Allen Probes data are obtained from: http://vanallenprobes.jhuapl.edu/index.php. GOES relativistic electron data are collected from: https://www.goes.noaa.gov/.

References

1. Abraham-Schrauner, B. (1972). Determination of magnetohydrodynamic shock normal. *Journal of Geophysical Research, 77*, 736-739. https://doi.org/10.1029/JA077i004p00736
2. Akasofu, S. I., & Chao, J. K. (1980). Interplanetary shock waves and magnetospheric substorms. *Planetary and Space Science, 28*, 381-385. https://doi.org/10.1016/0032-0633(80)90042-2
3. Allen, J., Sauer, H., Frank, L., & Reiff, P. (1989). Effects of the March 1989 solar activity. *Eos Transactions AGU, 70*, 1479-1488. https://doi.org/10.1029/89EO00409
4. Augusto, C. R. A., Navia, C. E., de Oliveira, M. N., Nepomuceno, A. A., Fauth, A. C., Kopenkin, V., & Sinzi, T. (2019). Relativistic proton levels from region AR 12673 (GLE #72) and the heliospheric current sheet as a Sun–Earth magnetic connection. *Publications of the Astronomical Society of the Pacific, 131*:024401. https://doi.org/10.1088/1538-3873/aaeb7f
5. Baker, D. N., Blake, J. B., Callis, L. B., Cummings, J. R., Hovestadt, D., Kanekal, S., Klecker, B., Mewaldt, R. A., & Zwickl, R. D. (1994). Relativistic electron acceleration and decay time scales in the inner and outer radiation belts: SAMPEX. *Geophysical Research Letters, 21*, 409-412. https://doi.org/10.1029/93GL03532

6. Baker, D. N., Jaynes, A. N., Li, X., Henderson, M. G., Kanekal, S. G., Reeves, G. D., Spence, H. E., Claudepierre, S. G., Fennell, J. F., Hudson, M. K., Thorne, R. M., Foster, J. C., Erickson, P. J., Malaspina, D. M., Wygant, J. R., Boyd, A., Kletzing, C. A., Drozdov, A., & Shprits, Y. Y. (2014). Gradual diffusion and punctuated phase space density enhancements of highly relativistic electrons: Van Allen Probes observations. *Geophysical Research Letters, 41*, 1351-1358. https://doi.org/10.1002/2013GL058942
7. Balogh, A., Bothmer, V., Crooker, N. U., Forsyth, R. J., Gloeckler, G., Hewish, A., Hilchenbach, M., Kallenbach, R., Klecker, B., Linker, J. A., Lucek, E., Mann, G., Marsch, E., Posner, A., Richardson, I. G., Schmidt, J. M., Scholer, M., Wang, Y. M., Wimmer-Schweingruber, R. F., Aellig, M. R., Bochsler, P., Hefti, S., & Mikić, Z. (1999). The solar origin of corotating interaction regions and their formation in the inner heliosphere. *Space Science Reviews, 89*, 141-178. https://doi.org/10.1023/A:1005245306874
8. Berdermann, J., Kriegel, M., Banyś, D., Heymann, F., Hoque, M. M., Wilken, V., Borries, C., Heßelbarth, A., & Jakowski, N. (2018). Ionospheric response to the X9.3 flare on 6 September 2017 and its implication for navigation services over Europe. *Space Weather, 16*, 1604-1615. https://doi.org/10.1029/2018SW001933
9. Boteler, D. H. (2003). Geomagnetic hazards to conducting networks. *Natural Hazards, 28*, 537-561. https://doi.org/10.1023/A:1022902713136
10. Burlaga, L. F., Ness, N. F., Mariani, F., Bavassano, B., Villante, U., Rosenbauer, H., Schwenn, R., & Harvey, J. (1978). Magnetic fields and flows between 1 and 0.3 AU during the primary mission of Helios 1. *Journal of Geophysical Research, 83*, 5167-5174. https://doi.org/10.1029/JA083iA11p05167
11. Burlaga, L. F., Sittler, E., Mariani, F., & Schwenn, R. (1981). Magnetic loop behind and interplanetary shock: Voyager, Helios and IMP-8 observations. *Journal of Geophysical Research, 6*, 6673-6684. https://doi.org/10.1029/JA086iA08p06673
12. Chamberlin, P. C., Woods, T. N., Didkovsky, L., Eparvier, F. G., Jones, A. R., Machol, J. L., Mason, J. P., Snow, M., Thiemann, E. M. B., Viereck, R. A., & Woodraska, D. L. (2018). Solar ultraviolet irradiance observations of the solar flares during the intense September 2017 storm period. *Space Weather, 16*, 1470-1487. https://doi.org/10.1029/2018SW001866
13. Chertok, I. M., Belov, A. V., & Abunin, A. A. (2018). Solar eruptions, Forbush decreases, and geomagnetic disturbances from outstanding active region 12673. *Space Weather, 16*, 1549-1560. https://doi.org/10.1029/2018SW001899
14. Clilverd, M. A., Rodger, C. J., Brundell, J. B., Dalzell, M., Martin, I., Mac Manus, D. H., Thomson, N. R., Petersen, T., & Obana, Y. (2018). Long-lasting geomagnetically induced currents and harmonic distortion observed in New Zealand during the 7-8 September 2017 disturbed period. *Space Weather, 16*, 704-717. https://doi.org/10.1029/2018SW001822
15. Cornwall, J. M. (1965). Cyclotron instabilities and electromagnetic emission in the ultra low frequency and very low frequency ranges. *Journal of Geophysical Research, 70*, 61-69. https://doi.org/10.1029/JZ070i001p00061
16. Domingo, V., Fleck, B. & Poland, A. I. (1995). The SOHO mission: an overview. *Solar Physics, 162*, 1-37. https://doi.org/10.1007/BF00733425
17. Dungey, J. W. (1961). Interplanetary magnetic field and the auroral zones. *Physical Review Letters, 6*, 47-48. https://doi.org/10.1103/PhysRevLett.6.47
18. Echer, E., Gonzalez, W. D., & Tsurutani, B. T. (2008). Interplanetary conditions leading to superintense geomagnetic storms (Dst ≤ -250 nT) during solar cycle 23. *Geophysical Research Letters, 35*, L06S03. https://doi.org/10.1029/2007GL031755

19. Echer, E., Tsurutani, B. T., & Guarnieri, F. L. (2009). Solar and interplanetary origins of the November 2004 superstorms. *Advances in Space Research, 44*, 615-620. https://doi.org/10.1016/j.asr.2009.05.003
20. Gjerloev, J. W. (2009). A global ground-based magnetometer initiative. *Eos Transactions AGU, 90*, 230-231. https://doi.org/10.1029/2009EO270002
21. Gonzalez, W. D., Tsurutani, B. T., Gonzalez, A. L. C., Smith, E. J., Tang, F., & Akasofu, S.-I. (1989). Solar wind-magnetosphere coupling during intense magnetic storms (1978-1979). *Journal of Geophysical Research, 94*, 8835-8851. https://doi.org/10.1029/JA094iA07p08835
22. Gonzalez, W. D., Joselyn, J. A., Kamide, Y., Kroehl, H. W., Rostoker, G., Tsurutani, B. T., & Vasyliunas, V. M. (1994). What is a geomagnetic storm? *Journal of Geophysical Research, 99*, 5771-5792. https://doi.org/10.1029/93JA02867
23. Gopalswamy, N., Lara, A., Yashiro, S., Kaiser, M. L., & Howard, R. A. (2001). Predicting the 1-AU arrival times of coronal mass ejections. *Journal of Geophysical Research, 106*, 29207-29217. https://doi.org/10.1029/2001JA000177
24. Hajra, R., & Tsurutani, B. T. (2018a). Interplanetary shocks inducing magnetospheric supersubstorms (SML < -2500 nT): unusual auroral morphologies and energy flow. *The Astrophysical Journal, 858*:123. https://doi.org/10.3847/1538-4357/aabaed
25. Hajra, R., & Tsurutani, B. T. (2018b). Magnetospheric "Killer" Relativistic Electron Dropouts (REDs) and Repopulation: A Cyclical Process. In *Extreme Events in Geospace: Origins, Predictability, and Consequences*, N. Buzulukova (Editor), Pages 373-400, Elsevier. https://doi.org/10.1016/B978-0-12-812700-1.00014-5
26. Hajra, R., Tsurutani, B. T., Echer, E., & Gonzalez, W. D. (2014). Relativistic electron acceleration during high-intensity, long-duration, continuous AE activity (HILDCAA) events: solar cycle phase dependences. *Geophysical Research Letters, 41*, 1876-1881. https://doi.org/10.1002/2014GL059383
27. Hajra, R., Tsurutani, B. T., Echer, E., Gonzalez, W. D., & Gjerloev, J. W. (2016). Supersubstorms (SML < -2500 nT): magnetic storm and solar cycle dependences. *Journal of Geophysical Research: Space Physics, 121*, 7805-7816. https://doi.org/10.1002/2015JA021835
28. Horne, R. B., Lam, M. M., & Green, J. C. (2009). Energetic electron precipitation from the outer radiation belt during geomagnetic storms. *Geophysical Research Letters, 36*, L19104. https://doi.org/10.1029/2009GL040236
29. Hudson, M. K., Baker, D. N., Goldstein, J., Kress, B. T., Paral, J., Toffoletto, F. R., & Wiltberger, M. (2014). Simulated magnetopause losses and Van Allen Probe flux dropouts. *Geophysical Research Letters, 41*, 1113-1118. https://doi.org/10.1002/2014GL059222
30. Illing, R. M. E., & Hundhausen, A. J. (1986). Disruption of a coronal streamer by an eruptive prominence and coronal mass ejection. Journal of Geophysical Research, 91, 10951-10960. https://doi.org/10.1029/JA091iA10p10951
31. Kanekal, S. G., Baker, D. N., Henderson, M. G., Li, W., Fennell, J. F., Zheng, Y., Richardson, I. G., Jones, A., Ali, A. F., Elkington, S. R., Jaynes, A., Li, X., Blake, J. B., Reeves, G. D., Spence, H. E., & Kletzing, C. A. (2015). Relativistic electron response to the combined magnetospheric impact of a coronal mass ejection overlapping with a high-speed stream: Van Allen Probes observations. *Journal of Geophysical Research: Space Physics, 120*, 7629-7641. https://doi.org/10.1002/2015JA021395
32. Kennel, C. F., & Petschek, H. E. (1966). Limit on stably trapped particle fluxes. *Journal of Geophysical Research, 71*, 1-28. https://doi.org/10.1029/JZ071i001p00001

33. Kennel, C. F., Edmiston, J. P., & Hada, T. (1985). A quarter century of collisionless shock research. In *Collisionless Shocks in the Heliosphere: A Tutorial Review*, edited by R. G. Stone and B. T. Tsurutani, American Geophysical Union, Washington, D.C. https://doi.org/10.1029/GM034p0001
34. Kessel, R. L., Fox, N. J., & Weiss, M. (2013). The Radiation Belt Storm Probes (RBSP) and space weather. *Space Science Reviews, 179*, 531-543. https://doi.org/10.1007/s11214-012-9953-6
35. Klein, L. W., & Burlaga, L. F. (1982). Interplanetary magnetic clouds at 1 AU. *Journal of Geophysical Research, 87*, 613-624. https://doi.org/10.1029/JA087iA02p00613
36. Kozyra, J. U., Liemohn, M. W., Cattell, C., De Zeeuw, D., Escoubet, C. P., Evans, D. S., Fang, X., Fok, M.-C., Frey, H. U., Gonzalez, W. D., Hairston, M., Heelis, R., Lu, G., Manchester IV, W. B., Mende, S., Paxton, L. J., Rastaetter, L., Ridley, A., Sandanger, M., Soraas, F., Sotirelis, T., Thomsen, M. W., Tsurutani, B. T., & Verkhoglyadova, O. (2014). Solar filament impact on 21 January 2005: Geospace consequences. *Journal of Geophysical Research: Space Physics, 119*, 5401-5448. https://doi.org/10.1002/2013JA019748
37. Lanzerotti, L. J. (1992). Comment on "Great magnetic storms" by Tsurutani et al. *Geophysical Research Letters, 19*, 1991-1992. https://doi.org/10.1029/92GL02238
38. Lemen, J. R., Title, A. M., Akin, D. J., et al. (2012). The Atmospheric Imaging Assembly (AIA) on the Solar Dynamics Observatory (SDO). *Solar Physics, 275*, 17-40. https://doi.org/10.1007/s11207-011-9776-8
39. Lepri, S. T., & Zurbuchen, T. H. (2010). Direct observational evidence of filament material within interplanetary coronal mass ejections. *The Astrophysical Journal, 723*, L22-L27. https://doi.org/10.1088/2041-8205/723/1/l22
40. Li, X., Baker, D. N., Temerin, M. A., Cayton, T. E., Reeves, E. G. D., Christensen, R. A., Blake, J. B., Looper, M. D., Nakamura, R., & Kanekal, S. G. (1997). Multi-satellite observations of the outer zone electron variation during the November 3-4, 1993, magnetic storm. *Journal of Geophysical Research, 102*, 14123-14140. https://doi.org/10.1029/97JA01101
41. Loomis, E. (1861). On the great auroral exhibition of Aug. 28th to Sept. 4, 1859, and on auroras generally. *American Journal of Science, 82*, 318-335. https://doi.org/10.2475/ajs.s2-32.96.318
42. Mauk, B. H., Fox, N. J., Kanekal, S. G., Kessel, R. L., Sibeck, D. G., & Ukhorskiy, A. (2013). Science objectives and rationale for the Radiation Belt Storm Probes Mission. *Space Science Reviews, 179*, 3-27. https://doi.org/10.1007/s11214-012-9908-y
43. Meng, X., Tsurutani, B. T., & Mannucci, A. J. (2019). The solar and interplanetary causes of superstorms (minimum Dst ≤ −250 nT) during the space age. *Journal of Geophysical Research: Space Physics, 124*. https://doi.org/10.1029/2018JA026425
44. Meredith, N. P., Cain, M., Horne, R. B., Thorne, R. M., Summers, D., & Anderson, R. R. (2003). Evidence for chorus-driven electron acceleration to relativistic energies from a survey of geomagnetically disturbed periods. *Journal of Geophysical Research, 108*, 1248. https://doi.org/10.1029/2002JA009764
45. Meurant, M., Gérard, J.-C., Blockx, C., Coumans, V., Hubert, B., Connors, M., Lyons, L. R., & Donovan, E. (2005). Comparison of intense nightside shock-induced precipitation and substorm activity. *Journal of Geophysical Research, 110*, A07228. https://doi.org/10.1029/2004JA010916
46. Michalek, G., Gopalswamy, N., Lara, A., & Manoharan, P. K. (2004). Arrival time of halo coronal mass ejections in the vicinity of the Earth. *Astronomy & Astrophysics, 423*, 729-736. https://doi.org/10.1051/0004-6361:20047184

47. Ness, N. F., & Wilcox, J. M. (1964). Solar origin of the interplanetary magnetic field. *Physical Review Letters, 13*, 461-464. https://doi.org/10.1103/PhysRevLett.13.461
48. Onsager, T., Grubb, R., Kunches, J., Matheson, L., Speich, D., Zwickl, R. W., & Sauer, H. (1996). Operational uses of the GOES energetic particle detectors. In *Proceedings SPIE 2812, GOES-8 and Beyond 281*. https://doi.org/10.1117/12.254075
49. Pirjola, R. (2000). Geomagnetically induced currents during magnetic storms. *IEEE Transactions on Plasma Science, 28*, 1867-1873. https://doi.org/10.1109/27.902215
50. Pizzo, V. J. (1985). Interplanetary shocks on the large scale: a retrospective on the last decade's theoretical efforts. In *Collisionless Shocks in the Heliosphere: Reviews of Current Research*, Geophysical Monograph Series, 35, edited by B. T. Tsurutani and R. G. Stone, 51-68, AGU, Washington, D.C. https://doi.org/10.1029/GM035p0051
51. Pulkkinen, A., Viljanen, A., Pajunpää, K., & Pirjola, R. (2001). Recordings and occurrence of geomagnetically induced currents in the Finnish natural gas pipeline network. *Journal of Applied Geophysics, 48*, 219-231. https://doi.org/10.1016/S0926-9851(01)00108-2
52. Redmon, R. J., Seaton, D. B., Steenburgh, R., He, J., & Rodriguez, J. V. (2018). September 2017's geoeffective space weather and impacts to Caribbean radio communications during hurricane response. *Space Weather, 16*, 1190-1201. https://doi.org/10.1029/2018SW001897
53. Remya, B., Tsurutani, B. T., Reddy, R. V., Lakhina, G. S., & Hajra, R. (2015). Electromagnetic cyclotron waves in the dayside subsolar outer magnetosphere generated by enhanced solar wind pressure: EMIC wave coherency. *Journal of Geophysical Research: Space Physics, 120*, 7536-7551. https://doi.org/10.1002/2015JA021327
54. Schillings, A., Nilsson, H., Slapak, R., Wintoft, P., Yamauchi, M., Wik, M., Dandouras, I., & Carr, C. M. (2018). O^+ escape during the extreme space weather event of 4-10 September 2017. *Space Weather, 16*, 1363-1376. https://doi.org/10.1029/2018SW001881
55. Seaton, D. B., & Darnel, J. M. (2018). Observations of an eruptive solar flare in the extended EUV solar corona. *The Astrophysical Journal Letters, 852*, L9. https://doi.org/10.3847/2041-8213/aaa28e
56. Sheeley, N. R., & Harvey, J. W. (1981). Coronal holes, solar wind streams, and geomagnetic disturbances during 1978 and 1979. *Solar Physics, 70*, 237-249. https://doi.org/10.1007/BF00151331
57. Shen, C., Xu, M., Wang, Y., Chi, Y., & Luo, B. (2018). Why the shock-ICME complex structure is important: learning from the early 2017 September CMEs. *The Astrophysical Journal, 861*:28. https://doi.org/10.3847/1538-4357/aac204
58. Smith, E. J. (1985). Interplanetary shock phenomena beyond 1 AU. In *Collisionless Shocks in the Heliosphere: Reviews of Current Research*, Geophysical Monograph Series, vol. 35, edited by B. T. Tsurutani and R. G. Stone, 69 pp., AGU, Washington, D. C. https://doi.org/10.1029/GM035p0069
59. Smith, E. J., & Wolfe, J. H. (1976). Observations of interaction regions and corotating shocks between one and five AU: pioneers 10 and 11. *Geophysical Research Letters, 3*, 137-140. https://doi.org/10.1029/GL003i003p00137
60. Smith, E. J., Tsurutani, B. T., & Rosenberg, R. L. (1978). Observations of the interplanetary sector structure up to heliographic latitudes of 16°: Pioneer 11. *Journal of Geophysical Research, 83*, 717-724. https://doi.org/10.1029/JA083iA02p00717
61. Sugiura, M. (1964). Hourly Values of Equatorial Dst for the IGY, Annual International Geophysical Year, vol. 35, p. 9, Pergamon, New York

62. Summers, D., Ni, B., & Meredith, N. P. (2007). Timescale for radiation belt electron acceleration and loss due to resonant wave-particle interactions: 2. Evaluation for VLF chorus, ELF hiss, and electromagnetic ion cyclotron waves. *Journal of Geophysical Research, 112*, A04207. https://doi.org/10.1029/2006JA011993
63. Tang, F., Tsurutani, B. T., Gonzalez, W. D., Akasofu, S. I., & Smith, E. J. (1989). Solar sources of interplanetary southward Bz events responsible for major magnetic storms (1978-1979). *Journal of Geophysical Research, 94*, 3535-3541. https://doi.org/10.1029/JA094iA04p03535
64. Thorne, R. M., & Kennel, C. F. (1971). Relativistic electron precipitation during magnetic storm main phase. *Journal of Geophysical Research, 76*, 4446-4453. https://doi.org/10.1029/JA076i019p04446
65. Tsurutani, B. T., & Gonzalez, W. D. (1987). The cause of high-intensity long-duration continuous AE activity (HILDCAAs): Interplanetary Alfvén wave trains. *Planetary and Space Science, 35*, 405-412. https://doi.org/10.1016/0032-0633(87)90097-3
66. Tsurutani, B. T., & Lin, R. P. (1985). Acceleration of > 47 keV ions and > 2 keV electrons by interplanetary shocks at 1 AU. *Journal of Geophysical Research, 90*, 1-11. https://doi.org/10.1029/JA090iA01p00001
67. Tsurutani, B. T., Gonzalez, W. D., Tang, F., Akasofu, S. I., & Smith, E. J. (1988). Origin of interplanetary southward magnetic fields responsible for major magnetic storms near solar maximum (1978-1979). *Journal of Geophysical Research, 93*, 8519-8531. https://doi.org/10.1029/JA093iA08p08519
68. Tsurutani, B. T., Gonzalez, W. D., Tang, F., & Lee, Y. T. (1992). Great magnetic storms. *Geophysical Research Letters, 19*, 73-76. https://doi.org/10.1029/91GL02783
69. Tsurutani, B. T., Gonzalez, W. D., Gonzalez, A. L. C., Tang, F., Arballo, J. K., & Okada, M. (1995). Interplanetary origin of geomagnetic activity in the declining phase of the solar cycle. *Journal of Geophysical Research, 110*, 21717-21733. https://doi.org/10.1029/95JA01476
70. Tsurutani, B. T., Gonzalez, W. D., Gonzalez, A. L. C., Guarnieri, F. L., Gopalswamy, N., Grande, M., Kamide, Y., Kasahara, Y., Lu, G., McPherron, R. L., Soraas, F., & Vasyliunas, V. (2006). Corotating solar wind streams and recurrent geomagnetic activity: a review. *Journal of Geophysical Research, 111*, A07S01. https://doi.org/10.1029/2005JA011273
71. Tsurutani, B. T., Echer, E., & Gonzalez, W. D. (2011). The solar and interplanetary causes of the recent minimum in geomagnetic activity (MGA23): a combination of midlatitude small coronal holes, low IMF Bz variances, low solar wind speeds and low solar magnetic fields. *Annales Geophysicae, 29*, 839-849. https://doi.org/10.5194/angeo-29-839-2011
72. Tsurutani, B. T., Hajra, R., Echer, E., & Gjerloev, J. W. (2015). Extremely intense (SML ≤ -2500 nT) substorms: isolated events that are externally triggered? *Annales Geophysicae, 33*, 519-524. https://doi.org/10.5194/angeo-33-519-2015
73. Tsurutani, B. T., et al. (2016). Heliospheric plasma sheet (HPS) impingement onto the magnetosphere as a cause of relativistic electron dropouts (REDs) via coherent EMIC wave scattering with possible consequences for climate change mechanisms. *Journal of Geophysical Research: Space Physics, 121*, 10130-10156. https://doi.org/10.1002/2016JA022499
74. Tsurutani, B. T., Park, S. A., Falkowski, B. J., Lakhina, G. S., Pickett, J. S., Bortnik, J., Hospodarsky, G., Santolik, O., Parrot, M., Henri, P., & Hajra, R. (2018). Plasmaspheric hiss: coherent and intense. Journal of Geophysical Research: Space Physics, 123, 10009-10029. https://doi.org/10.1029/2018JA025975

75. Van Allen, J. A., & Frank, L. A. (1959). Radiation measurements to 658,300 km with Pioneer IV. *Nature, 184*, 219-224. https://doi.org/10.1038/184219a0
76. Viljanen, A., Nevanlinna, H., Pajunpää, K., & Pulkkinen, A. (2001). Time derivative of the horizontal geomagnetic field as an activity indicator. *Annales Geophysicae, 19*, 1107-1118. https://doi.org/10.5194/angeo-19-1107-2001
77. Viljanen, A., Pulkkinen, A., Pirjola, R., Pajunpää, K., Posio, P., & Koistinen, A. (2006). Recordings of geomagnetically induced currents and a nowcasting service of the Finnish natural gas pipeline system. *Space Weather, 4*, S10004. https://doi.org/10.1029/2006SW000234
78. Wanliss, J. A., & Showalter, K. M. (2006). High-resolution global storm index: Dst versus SYM-H. *Journal of Geophysical Research, 111*, A02202. https://doi.org/10.1029/2005JA011034
79. West Jr., H. I., Buck, R. M., & Walton, J. R. (1972). Shadowing of electron azimuthal-drift motions near the noon magnetopause. *Nature Physical Science, 240*, 6-7. https://doi.org/10.1038/physci240006a0
80. Winterhalter, D., Smith, E. J., Burton, M. E., Murphy, N., & McComas, D. J. (1994). The heliospheric plasma sheet. *Journal of Geophysical Research, 99*, 6667-6680. https://doi.org/10.1029/93JA03481
81. Yan, X. L., Wang, J. C., Pan, G. M., Kong, D. F., Xue, Z. K., Yang, L. H., Li, Q. L., & Feng, X. S. (2018). Successive X-class flares and coronal mass ejections driven by shearing motion and sunspot rotation in active region NOAA 12673. *The Astrophysical Journal, 856*:79. https://doi.org/10.3847/1538-4357/aab153
82. Zhang, J., Richardson, I. G., Webb, D. F., Gopalswamy, N., Huttunen, E., Kasper, J. C., Nitta, N. V., Poomvises, W., Thompson, B. J., Wu, C. C., Yashiro, S., Zhukov, A. N. (2007). Solar and interplanetary sources of major geomagnetic storms (Dst ≤ −100 nT) during 1996-2005. *Journal of Geophysical Research, 112*, A10102. https://doi.org/10.1029/2007JA012321
83. Zhou, X., & Tsurutani, B. T. (2001). Interplanetary shock triggering of nightside geomagnetic activity: substorms, pseudobreakups, and quiescent events. *Journal of Geophysical Research, 106*, 18957-18967. https://doi.org/10.1029/2000JA003028
84. Zhou, G., Wang, J., & Cao, Z. (2003). Correlation between halo coronal mass ejections and solar surface activity. *Astronomy & Astrophysics, 397*, 1057-1067. https://doi.org/10.1051/0004-6361:20021463
85. Zou, P., Jiang, C., Feng, X., Zuo, P., Wang, Y., & Wei, F. (2019). A two-step magnetic reconnection in a confined X-class flare in solar active region 12673. *The Astrophysical Journal, 870*:97. https://doi.org/10.3847/1538-4357/aaf3b7

Tables

Table 1. X-class solar flares recorded during September 2017

Flare no.	Date	Start time (UT)	Peak time (UT)	End time (UT)	Class	Location
XFlare1	06/09	08:57	09:10	09:17	X2.2	S08W33
XFlare2	06/09	11:53	12:02	12:10	X9.3	S08W33
XFlare3	07/09	14:20	14:36	14:55	X1.3	S11W49
XFlare4	10/09	15:35	16:06	16:31	X8.2	S14W74

Table 2. Propagation prediction of halo CMEs to the Earth

CME no.	CME time (UT)	V_{CME} (km s^{-1})	Predicted time at 1 AU (UT)			Observed FS time at 1 AU (UT)	Error (h)		
			Mod1	Mod2	Mod3		Mod1	Mod2	Mod3
hCME1	04/09 20:36	1418	06/09 11:46	06/09 09:50	06/09 19:55	06/09 23:02	11.4	13.3	3.2
hCME2	06/09 12:24	1571	07/09 22:48	07/09 21:36	08/09 04:34	07/09 22:19	-0.4	0.6	-6.3
hCME3	10/09 16:00	3163	11/09 06:58	11/09 07:12	11/09 07:55	12/09 19:12	36.3	36.1	35.4
hCME4	17/09 12:00	1385	19/09 04:19	19/09 02:10	19/09 13:12	No significant ICME signature			

Table 3. Characteristics of the interplanetary discontinuities at WIND spacecraft

Time (UT)	Type	Jump in interplanetary parameters					θ_{Bn} (°)	MMN	Impacts
		Vsw (km s^{-1})	Nsw (cm^{-3})	Psw (nPa)	Tsw (10^4 K)	Bo (nT)			
06/09 23:02	FS1	410-575	2-14	2-13	2-40	2-6	89.8	5.80	SI+ ~+56 nT
07/09 22:19	FS2	475-680	3-4	2-9	2-80	10-22	47.9	6.73	SI+ ~+20 nT, SSS (SME 4464 nT, SML -3712 nT)
12/09 19:12	FS3	460-620	5-17	2-16	12-56	4-8	19.4	3.97	SI+ ~+27 nT, substorm (SME 1366 nT, SML -1071 nT)
14/09 00:00	FS4	350-370	5-12	1-4	3-8	2-5	8.5	4.30	SI+ ~+14 nT
14/09 10:05	FS5	345-419	10-33	2-9	7-9	2-4	84.0	1.73	SI+ ~+28 nT
14/09 14:10	HCS1	436-474	11-40	4-20	11-37	4-10			Substorm (SME 1171 nT, SML -766 nT)
14/09 18:29	RW1	473-630	11-4	15-2	36-19	10-5	71.2	0.84	SI- ~-23 nT, substorm recovery
24/09 21:22	HCS2	330-370	5-36	1-7	2-5	4-9			No substorm
26/09 22:48	FS6	310-333	13-21	2-6	1-5	4-7	33.5	2.72	SI+ ~+14 nT
27/09 05:17	HCS3	350-530	18-54	4-14	4-40	9-16			Substorm (SME 883 nT, SME -614 nT) (07:39)
28/09 08:38	RW2	651-692	7-4	7-2	37-25	7-3	86.7	0.71	SI- ~-14 nT, substorm recovery

Table 4. Interplanetary sheaths and MCs

Type	Start time (UT)	End time (UT)	Peak IMF Bz (nT)	Impacts
Sheath1	06/09 23:02	07/09 22:19	-11	Substorm (SME 1417 nT, SML -1097 nT)
Sheath2	07/09 22:19	08/09 11:02	-31	Intense storm (SYM-H -146 nT), SSS (SME 4464 nT, SML -3712 nT)
MC	08/09 11:02	11/09 00:43	-17	Intense storm (SYM-H -115 nT), SSS (SME 4330 nT, SML -2642 nT)
Sheath3	12/09 19:12	13/09 03:22	-12	Moderate storm (SYM-H -65 nT), substorm (SME 1366 nT, SML -1071 nT), substorm (SME 1856 nT, SML -1541 nT)
Sheath4	14/09 00:00	14/09 10:05	-4	Substorm (SME 389 nT, SML -306 nT)

Table 5. Interplanetary HSSs and CIRs

Type	Start time (UT)	End time (UT)	Vsw (km s^{-1})	Impacts
HSS1	01/09 04:09	02/09 23:18	687	Intense auroral (SME ~1588 nT, SML ~-1439 nT) activity
HSS2	14/09 18:43	18/09 22:29	743	Intense auroral (SME ~1749 nT, SML ~-1423 nT) activity
HSS3	27/09 15:41	29/09 22:16	721	Intense auroral (SME ~2044 nT, SML ~-949 nT) activity
CIR1	14/09 10:05	14/09 18:29	333-743	No storm/substorm
CIR2	26/09 22:48	28/09 08:38	315-721	Moderate storm (SYM-H -74 nT), substorm (SME 2683 nT, SML -1813 nT)

Table 6. SSSs and GICs

SSS no.	SSS interval		SSS strength		GIC impact	
	Start (UT)	End (UT)	SML peak	Time (UT)	GIC peak (A)	Time (LT)
SSS1	07/09 22:19	08/09 02:51	-3712	08/09 00:24	28.2	08/09 03:31
SSS2	08/09 11:34	08/09 15:42	-2642	08/09 13:08	30.4	08/09 20:55

Figures and Captions

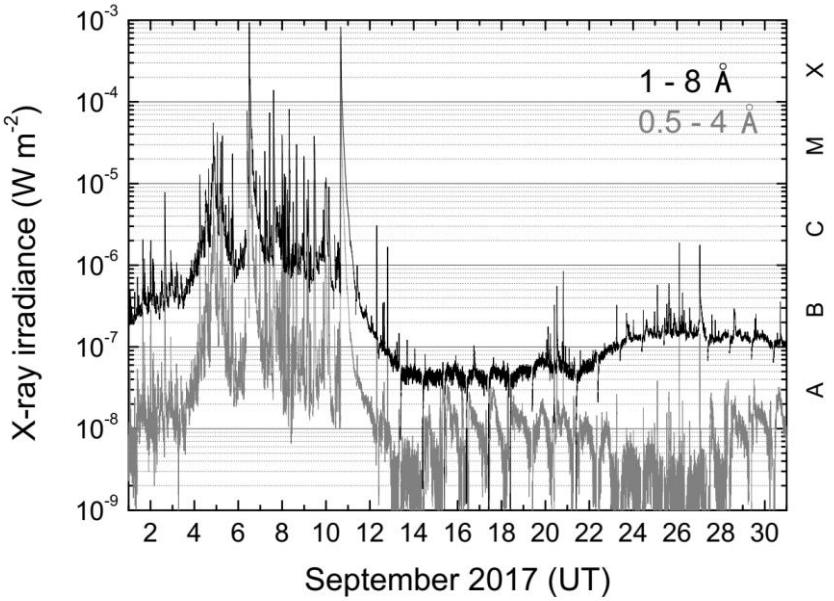

Figure 1. The GOES x-ray irradiance during September 2017. Classes of x-ray flares are marked on the right.

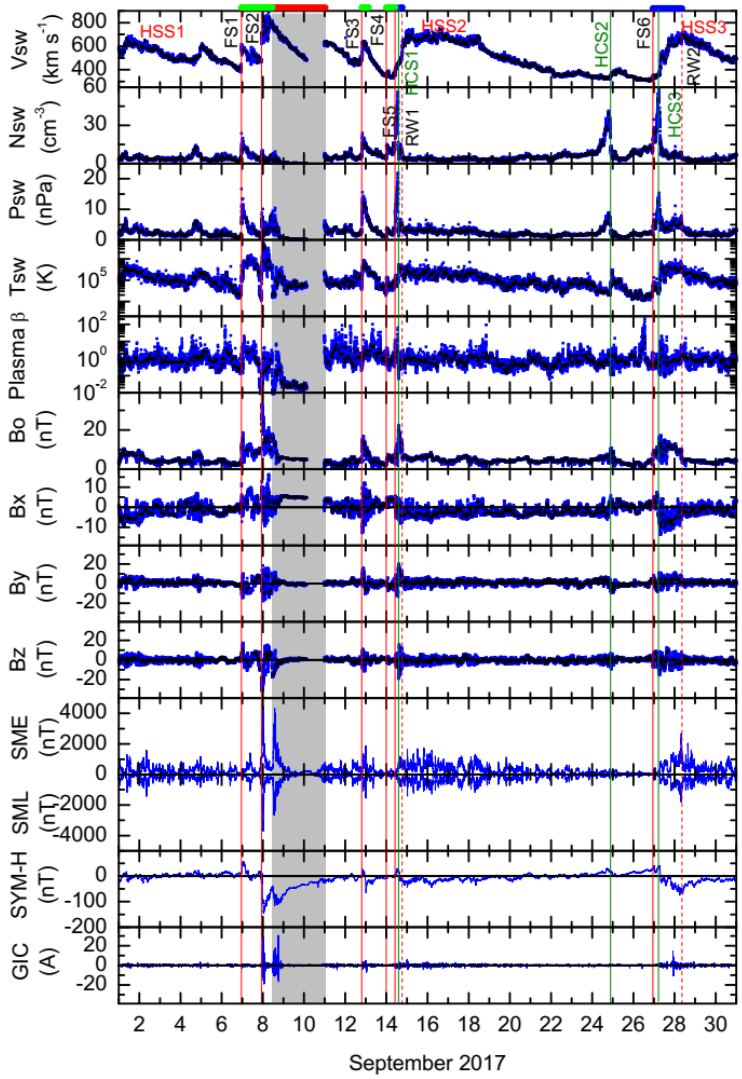

Figure 2. Solar wind/interplanetary and geomagnetic variations during September 2017. From top to bottom, the panels show the solar wind plasma speed (Vsw), density (Nsw), ram pressure (Psw), plasma temperature (Tsw), plasma beta (β), interplanetary magnetic field (IMF) amplitude Bo, and Bx, By, Bz components in geocentric solar magnetospheric (GSM) coordinate system, auroral electrojet SME and SML indices, symmetric ring current SYM-H index, and geomagnetically induced current (GIC), respectively. The blue and black data points correspond to 1 min and 1 h resolution, respectively. Vertical red solid, red dashed and green solid lines indicate FSs, RWs and HCSs, respectively. On the top, green, red and blue horizontal bars indicate the interplanetary sheath, MC and CIR intervals, respectively.

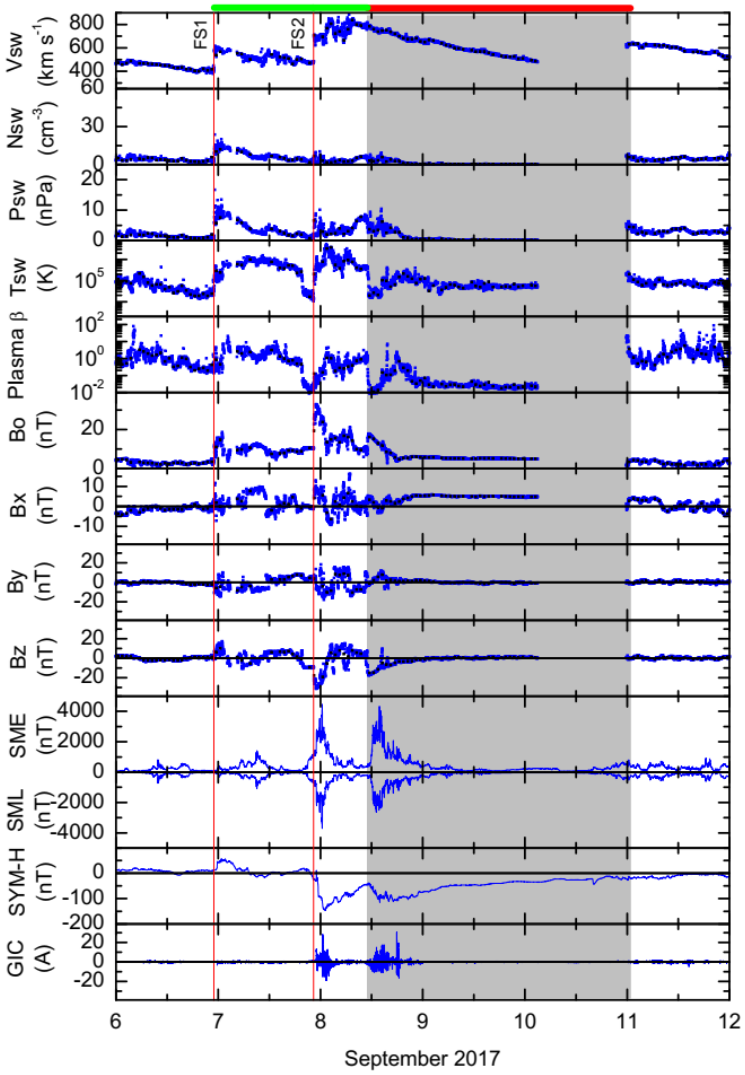

Figure 3. Solar wind/interplanetary and geomagnetic variations during 6 – 11 September 2017. The panels are in same format as in Figure 2.

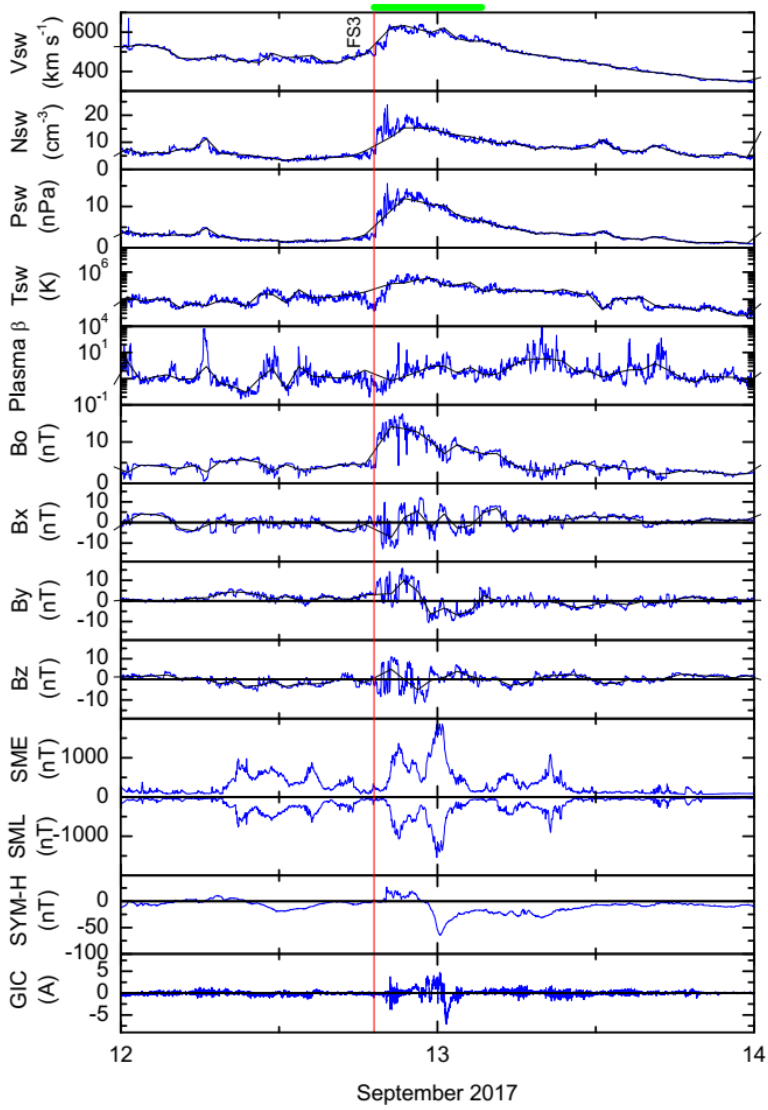

Figure 4. Solar wind/interplanetary and geomagnetic variations during 12 – 13 September 2017. The panels are in same format as in Figure 2.

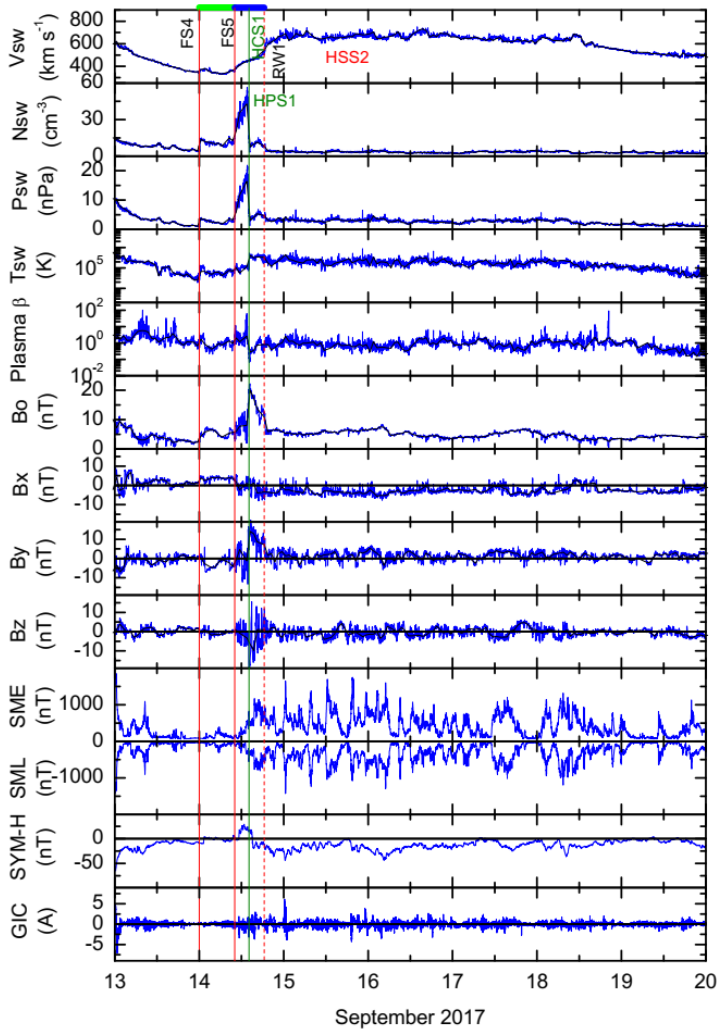

Figure 5. Solar wind/interplanetary and geomagnetic variations during 13 – 19 September 2017. The panels are in same format as in Figure 2.

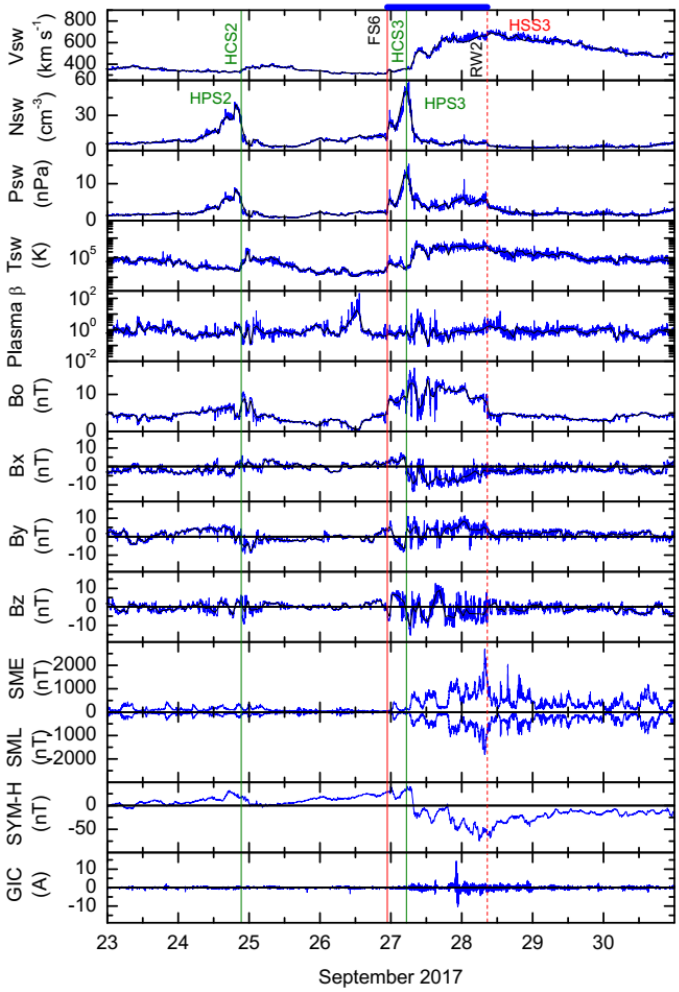

Figure 6. Solar wind/interplanetary and geomagnetic variations during 23 – 30 September 2017. The panels are in same format as in Figure 2.

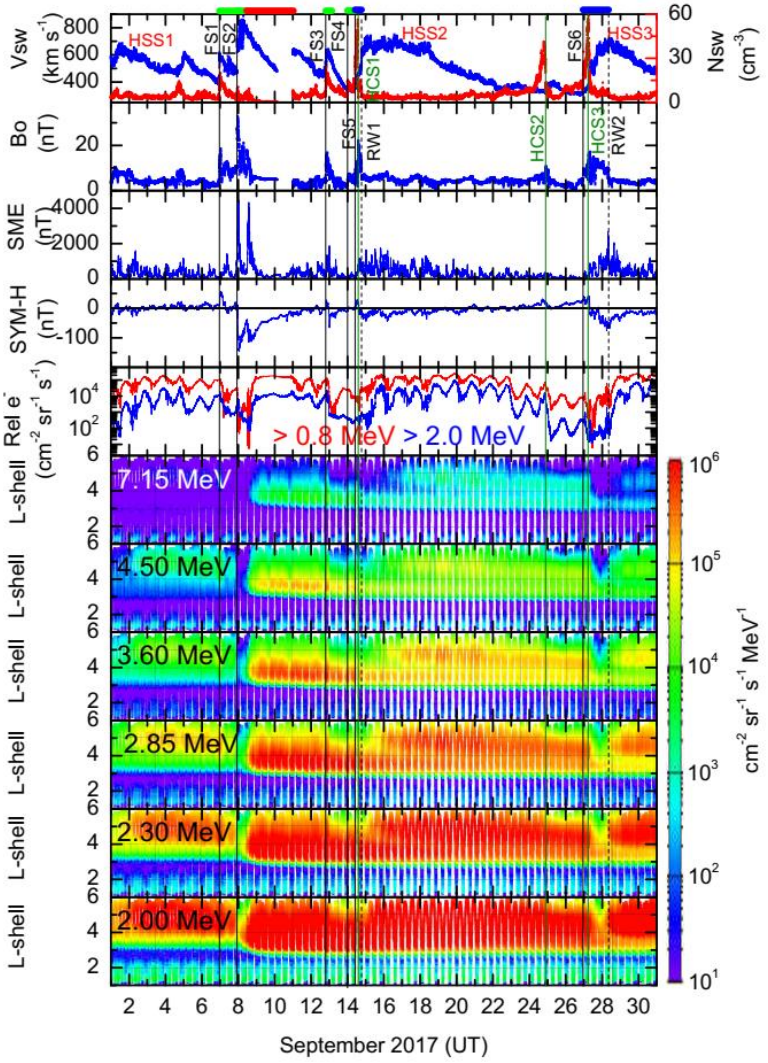

Figure 7. Response of the outer zone radiation belt relativistic electron fluxes to the complex and multiple space weather events. In the top four panels interplanetary and geomagnetic data from Figure 2 are repeated to give reference to interplanetary and geomagnetic events. The fifth panel from the top displays relativistic > 0.8 MeV and > 2.0 MeV electron fluxes at geosynchronous GOES 15 orbit. The bottom six panels show the L-shell variations of 7.15 MeV, 4.50 MeV, 3.60 MeV, 2.85 MeV, 2.30 MeV and 2.00 MeV electron fluxes measured by the REPT instrument on VAPs, respectively. Flux values are shown in the colour scale on the right. Vertical black solid, black dashed and green solid lines indicate FSs, RWs and HCSs, respectively. On the top, green, red and blue horizontal bars indicate the interplanetary sheath, MC and CIR intervals, respectively.